Proudman Oceanographic Laboratory
NATURAL ENVIRONMENT RESEARCH COUNCIL

Effect of coastal boundary resolution and mixing upon internal wave generation and propagation in coastal regions.

P. Hall *, A.M. Davies
Proudman Oceanographic Laboratory, 6 Brownlow Street, Liverpool L3 5DA, UK.

Abstract

A non–linear two–dimensional vertically stratified cross–sectional model of a constant depth basin without rotation is used to investigate the influence of vertical and horizontal diffusion upon the wind–driven circulation in the basin and the associated temperature field. The influence of horizontal grid resolution, in particular the application of an irregular grid with high resolution in the coastal boundary layer is examined. The calculations show that the initial response to a wind impulse is downwelling at the downwind end of the basin with upwelling and convective mixing at the opposite end. Results from a two–layer analytical model show that the initial response is the excitation of an infinite number of internal seiche modes in order to represent the initial response which is confined to a narrow near coastal region. As time progresses, at the downwind end of the basin a density front propagates away from the boundary, with the intensity of its horizontal gradient and associated vertical velocity determined by both horizontal and vertical viscosity values. Calculations demonstrate the importance of high horizontal grid resolution in resolving this density gradient together with an accurate density advection scheme. The application of an irregular grid in the horizontal with high grid resolution in the nearshore region enables the initial response to be accurately reproduced although physically unrealistic short waves appear as the frontal region propagates onto the coarser grid. Parameterization of horizontal viscosity using a Smagorinsky–type formulation acts as a selective grid size–dependent filter, and removes the short–wave problem although enhanced smoothing can occur if the scaling coefficient in the formulation is too large. Calculations clearly show the advantages of using an irregular grid but also the importance of using a grid size–dependent filter to avoid numerical problems.

1. INTRODUCTION

The problem of determining the wind–induced response of a sea region or lake, particularly in stratified conditions, has been an important and long–standing issue in physical oceanography. Early work by Platzman (1963) showed that strong–wind bursts could excite seiches in lakes with associated changes in surface elevation. In its simplest form, the lowest mode seiche is a free oscillation involving water movement from one end of a lake to another. When the lake is stratified, topographic and rotation effects are important and the response is very complex. Analytical work (Csanady 1972, 1973) investigated the problem of the wind response of constant–depth circular and rectangular lakes with linear stratification in the vertical (Csanady 1972) or in terms of two layers (Csanady 1973). Calculations with a circular lake showed that at the coastal boundary there were narrow (of order 5 km) "coastal jets", with Poincaré–type waves in the centre. In the case of a rectangular lake, depending upon its characteristics, odd number seiches are generated (Csanady 1973). In a narrow lake (Heaps and Ramsbottom 1966, hereafter HR66), rotational effects are less important and can often be neglected. In such cases the response of the region to a wind blowing along the axis of the lake is downwelling at the downwind end of the lake, with upwelling at the opposite end as described in Csanady (1973). At the upwelling end, denser water is moved into the surface layer, and convective mixing occurs giving rise to a stable water column. Later in this article, we show that this gives rise to a relatively wide well–mixed coastal region. However, at the downwelling end, lighter water is moved to depth in a narrow coastal layer. As the wind forcing decreases, the vertical displacement of the density surfaces is reduced by the restoring force of gravity, and internal waves with associated fronts (Simons 1978) propagate from the

* Corresponding author.
Email address: phh@pol.ac.uk (P. Hall).

lateral boundaries into the interior of the region. Owing to the differences in mixing at upwind and downwind coastal boundaries the response is not anti–symmetric, and consequently, there are differences in the propagation of internal waves from each boundary into the interior. In larger lakes, rotational effects are important and can influence the wind–induced circulation (Winant 2004). A detailed review of the response of lakes to wind forcing is given in Csanady (1996). The response of a large sea region such as the North Sea [the northern part of which has water depths of the order of 250 m, and is stratified in summer (Heaps 1980)] is the initial breakdown of the summer stratification in the autumn time, and the generation of major stormsurges in response to winter storms. In such a region, rotational effects are important and influence the depth of penetration of the winds energy, and the generation of inertial oscillations and internal waves with strong shear at the level of the thermocline which are important in deepening the thermocline.

The objective of the present paper is to use a three–dimensional non–linearmodel [which has been extensively applied in realistic sea regions (Xing and Davies 2001b; Xing et al. 1999)] in cross–sectional form, to examine the importance of horizontal grid resolution, (particularly in near coastal regions where the internal waves are produced) upon the generation and propagation of internal waves. The effect of the value of horizontal diffusion upon this propagation is also considered. The model has a uniform finite difference grid in the horizontal which can be refined in the coastal region by the use of a transformation factor. The influence of a near coastal grid enhancement upon the stability of the solution is also examined. Diffusion in the vertical is parameterized by either a fixed diffusion coefficient or one computed from a turbulence energy closure model. The effect of changing the magnitude of the horizontal and vertical diffusion coefficient upon the width of the coastal boundary layer, and hence the grid resolution required to resolve this layer and the subsequent offshore propagation of internal waves is examined. In addition, the importance of horizontal resolution and offshore propagation of internal waves upon the vertical diffusion computed with the turbulence energy model is also considered. The importance of including seiche motion within a turbulence energy model applied in lake conditions was recently shown by Goudsmit et al. (2002). In a more general context, Davies and Xing (2003) for stratified seas and Xing and Davies (2005) for a cold–water dome, recently showed the importance of including internal–wave propagation within a turbulence energy model in order to simulate mixing within the thermocline. The sensitivity and numerical stability of the solution to changes in grid resolution and parameterization of diffusion is examined in detail.

In essence, the focus of the paper is twofold: Primarily to examine the accuracy and stability of a non–uniform grid, (achieved by a transformation technique) when applied to internal–wave generation and propagation in a non–linear hydrodynamic model; Secondly to examine the sensitivity of the solution to the parameterization of vertical and horizontal mixing and how this impacts upon the accuracy and stability of the solution. To determine these effects, a detailed comparison is made with a high accuracy non–linear solution derived on a fine uniform grid, namely, a benchmark solution. In addition the analytical solution of the linear problem is used to yield insight into the importance of boundary–layer resolution.

The form of the three–dimensional model and turbulence closure model with brief details of their numerical solution is given in the next section. In section three an analytical solution of a cross–sectional linear model to a wind pulse is presented to yield some insight into the importance of resolution in coastal boundary layers upon the wind–induced response of a sea region. In subsequent sections, the numerical results of the nonlinear problem with a range of uniform and non–uniform grids are presented and compared with an accurate solution, with conclusions given in a final section.

2. The three–dimensional non–linear numerical model.

The continuity equation, momentum equations, and transport equations for temperature using Cartesian coordinates in the horizontal and σ coordinates in the vertical, where $\sigma = (z–\zeta)/H$ with σ=0 sea surface and σ = –1 the sea bed, are given by

$$\frac{\partial \zeta}{\partial t} + \nabla \cdot \left(\int_{-1}^{0} (H\overrightarrow{V}) d\sigma \right) = 0 \tag{1}$$

$$\frac{\partial Hu}{\partial t} + S_u - fHv = -gH\frac{\partial \zeta}{\partial x} + BPF_x + \frac{1}{H^2}\frac{\partial}{\partial \sigma}\left(A_v \frac{\partial Hu}{\partial \sigma} \right) + D_u \tag{2}$$

$$\frac{\partial Hv}{\partial t} + S_v + fHu = -gH\frac{\partial \zeta}{\partial y} + BPF_y + \frac{1}{H^2}\frac{\partial}{\partial \sigma}\left(A_v \frac{\partial Hv}{\partial \sigma} \right) + D_v \tag{3}$$

The vertical velocity ω, which appears in the three–dimensional advection terms, is obtained diagnostically from the continuity equation (Xing and Davies 2001b), with the pressure P at any depth σ given by

$$\frac{\partial P}{\partial \sigma} = -\rho g H \tag{4}$$

The time evolution of temperature T is given by

$$\frac{\partial HT}{\partial t} + S_T = \frac{1}{H^2}\frac{\partial}{\partial \sigma}\left(K_v \frac{\partial HT}{\partial \sigma} \right) + D_T \tag{5}$$

A simple equation of state was used to convert temperature into density, namely $\rho = \rho_0[1 - \beta(T - T_0)]$, with β=0.0002/°C and T_0 a reference temperature corresponding to ρ_0.

In these equations, $\overrightarrow{V} = (u, v)$ and (u, v, ω) are the velocity components corresponding to the (x, y, σ) coordinates: ρ is density; T is the temperature; $H = h + \zeta$ is the water depth; f is the elevation of the sea surface above the undisturbed level h; z is the water depth increasing vertically upwards with $z = \zeta$ the free surface and $z = -h$ the sea bed; f is the Coriolis parameter, g is the gravitational acceleration; t is time; with BPF_x, BPF_y being the baroclinic pressure force terms (see Xing and Davies 1998, 2001b; Xing et al. 1999, for details). The terms S_U, S_V, S_T represent the full three–dimensional momentum advection terms, with D_U, D_V, D_T the horizontal diffusion terms. Details of the mathematical formulation of these terms are given in Xing and Davies (2001b). Horizontal viscosity (A_m) and diffusivity (A_h) were given by A_m=100 m^2 s^{-1} and A$_h$=100 m^2 s^{-1}. The influence of determining A_m using a Smagorinsky (1963) formulation (Blumberg and Mellor 1987) is given by

$$A_m = C\Delta x\Delta y\left[\left(\frac{\partial u}{\partial x}\right)^2 + \frac{1}{2}\left(\frac{\partial v}{\partial x} + \frac{\partial u}{\partial y}\right)^2 + \left(\frac{\partial v}{\partial y}\right)^2\right]^{\frac{1}{2}} \quad (6)$$

with C an arbitrary scaling coefficient, and $\Delta x, \Delta y$ horizontal grid spacing was also considered. The vertical eddy viscosity and diffusivity are denoted by A_v, K_v. In some calculations these were specified, in others they were computed using a turbulence energy sub–model Xing and Davies (1998, 2001b); Luyten et al. (1996, 2002); Bolding et al. (2002).At the land boundary the normal component of flow was set to zero. At the seabed a linear friction law was applied with a coefficient K=0.0005 m s^{-1}, an appropriate value in a shallow region. For temperature the heat flux was zero at sea surface and sea bed. The surface stress was set equal to the wind stress. In all calculations described subsequently the wind stress was increased sinusoidally from 0.0 Pa at t=0, to 0.5 Pa at t=6 h with a similar reduction to zero at t=12 h, after which the stress was zero. This was chosen to be consistent with Davies (1980) who used a functional model to examine the wind–induced response of the linear form of the hydrodynamic equations given here. In that model, as in the analytical solution of HR66 there was no temperature mixing, although temperature advection occurred. Although details of the numerical solution of these equations is given in Xing and Davies (2001b,a), it is worth stressing that temperature advection was solved using a total variation diminishing (TVD) scheme described by James (1996). This method has been very successful in advecting sharp density gradients associated with internal tides over steep topography (Xing and Davies 1998). By comparing the numerical solution derived here, using a range of uniform and variable grids, against an accurate solution derived with a high resolution fine grid (the benchmark solution), the influence of grid resolution upon accuracy and stability can be determined. In addition, by using a range of mixing coefficient values and parameterizations, their influence upon the grid resolution required to achieve an accurate and stable solution can be determined. The analytical solution of HR66 and its application to a wind impulse problem (Davies 1980) are used to give insight into the nature of the physics determining the solution, and the numerical implications of the time decay of the solution. In the calculations described later in order to examine the wind–induced response of the upwind and downwind boundaries separately and make comparisons with an earlier calculation (Davies 1980) a cross–sectional model of the North Sea was used. To be consistent with Davies (1980) and the analytical solution of HR66, rotational effects were removed so that the model had "lake–like" characteristics, but the two boundaries were sufficiently well removed that they could be studied separately. Consequently, in the calculations described subsequently, the three–dimensional model was used in cross–sectional form with f=0. Hence there was no y dependency of the solution, and v=0 throughout. Unlike in the analytical solutions of HR66 (see below) or the numerical solution of Davies (1980), vertical mixing of temperature is allowed in the present model. Hence besides advection of the temperature field by the wind–induced circulation, a surface–mixed layer and diffusion and mixing of the thermocline can occur in response to wind forcing. This will be discussed more in connection with the calculations.

3. Analytical solution

In order to gain some insight into the accuracy of the numerical model and appreciate the processes giving rise to the flow fields in the model, it is useful to compare the solution with that derived analytically from a two–layer model. By approximating the density distribution used in the numerical model, by two homogeneous layers of thickness h_1 and h_2 with density ρ_1 and ρ_2, an analytical solution of the linear equations (HR66) for the free periods of both the surface and interface displacement can be obtained. In this solution, interfacial friction is assumed to be zero (HR66) although bottom friction is included. One important difference between layered and continuous models is that in a two–layered model only the surface mode and the first internal mode together with their higher harmonics can be generated, whereas in a continuously stratified basin, an infinite number of internal modes with higher harmonics is possible.

Without bottom friction, analytical solutions giving the periods of the surface modes,

$$T_n = \frac{1}{n}\frac{2l}{C_1}, \text{with } C_1 = (gh)^{1/2} \text{ where } n = 1, 2, ...\infty, \quad (7)$$

with l basin length taken as 400 km and the first internal mode

$$T_n = \frac{1}{n}\frac{2l}{C_2}, \text{with } C_2 \quad (8)$$

$$= \left[g \frac{h_1 h_2}{h} \left(\frac{\rho_2 - \rho_1}{\rho_2} \right) \right]^{\frac{1}{2}} \text{where } n = 1, 2, ...\infty,$$

can be obtained (HR66).

From Eq. 8 it is evident that the period of the internal seiche will be highly sensitive to density differences between the upper and lower layers. Approximating the density distribution used in the numerical model, by two layers h_1=55 m, h_2=195 m, with ρ_1=1026.3 Kg m^{-3} and ρ_2=1027.5 Kg m^{-3} (see Fig. 1) gives using Eq. 8 a first internal mode seiche period of T_1=317 h.

For the case in which internal displacements are generated by a suddenly imposed wind stress given by,

$$F_S = H(t) \sum_{n=1}^{\infty} A_n sin(\frac{n\pi x}{l}), \tag{9}$$

it is possible to derive an analytical solution (Heaps and Ramsbottom 1966), for ζ_2 (the vertical displacement of the interface between the layers in the two–layered model), of the form,

$$\zeta_2 = H(t) \sum_{n=1}^{\infty} Z_2^{(n)} cos(\frac{n\pi x}{l}) \tag{10}$$

In Eqs. 9, 10 and 11, A_n is a constant, $H(t)$ is the Heavyside unit function, and K is the coefficient of bottom friction in the two–layer model. If the effect of friction upon σ_n is small, then Eq. 10 can be further simplified by assuming $\sigma_n = C_2$ for all n (Heaps and Ramsbottom 1966).

Fourier decomposition of the wind stress used in the numerical model yields,

$$F_2(x) = \sum_{n=1}^{\infty} A_n sin \frac{n\pi x}{l} \tag{11}$$

where

$$A_n = \begin{cases} 4/n\pi & (n\,odd) \\ 0 & (n\,even) \end{cases} \tag{12}$$

Consequently only surface and internal seiches with n odd will be present in the numerical solution.

The analytical solution presented above is for a suddenly applied and maintained wind stress. However, as shown by Davies (1980), this can be applied to a wind pulse of duration Δt by linearly combining this solution with one corresponding to a suddenly applied wind stress in the opposite direction, shifted in time by Δt. Since the analytical model is linear and only used here to understand the implications of physical processes upon the basin circulation and numerical solution, the solution of Davies (1980) is sufficiently accurate to facilitate this. However, an accurate numerical solution of the full nonlinear model (termed the benchmark solution, see below) is required to quantify the accuracy of the various grids.

4. Numerical calculations.

4.1. *The "benchmark" calculation with fixed diffusion coefficients*

Results from the analytical solution presented previously for a two–layered linear model (in which there was no vertical diffusion) showed that the initial response was a narrow coastal region of significant downwelling at the downwind end of the basin. The linear nature of the solution and lack of mixing meant that there was an associated identical upwelling at the other end of the basin (Davies 1980).

In the analytical model, the presence of the up– and downwelling regions confined on the short time scale to the coastal boundary, with no vertical motion outside this boundary layer, was represented by an infinite number of internal modes. As time progresses, the higher–order modes are damped more rapidly than the lower modes as the region of up– and downwelling spreads from the boundary into the interior. Since the spatial variability of lower modes is significantly less than for the higher modes, then as time progresses, the solution will exhibit less horizontal spatial variability and a coarser grid should be adequate. The analytical solution therefore suggests that the crucial test of accuracy is the near coastal response on the short time scale.

In order to examine if this conclusion holds in the non–linear numerical model and to understand the influence of variable grid resolution, and parameterization of diffusion upon the solution, an initial high resolution "benchmark" (BM) solution was developed with a uniform finite difference grid resolution of order of 60 m.

In this initial "benchmark" calculation (Calc BM, Table 1), following Xing and Davies (2001b,a), 27 sigma levels were used in the vertical, with enhanced resolution in the surface wind driven high shear layer. The density and eddy viscosity profiles (an identical eddy diffusivity was used) were as shown in Fig. 1, and corresponded to those used by Davies (1980). Horizontal eddy viscosity was taken as A_m=100 m^2 s^{-1} with diffusivity A_h=100 m^2 s^{-1}. The wind forcing and water depth together with basin dimension were identical to those used in the analytical and numerical solutions of Davies (1980). These parameters were fixed in all calculations unless stated otherwise.

The initial (up to 10 h) wind–forced response (Fig. 2) is a surface wind–driven current, with downwelling at the downwind end of the basin, and upwelling at the opposite end. This gives a near coastal displacement of the temperature surfaces and weak return flow at depth. The circulation in the basin is shown by the streamlines (Fig. 2, t=10 h), with closely spaced streamlines indicating stronger currents.

At the downwind (eastern) end of the basin, the wind-forced flow leads to a downwelling of the temperature surfaces in a region of the order of a couple of horizontal grid boxes wide. The resulting horizontal temperature gradient gradually propagates westward (Fig. 2, t=20 h) away from

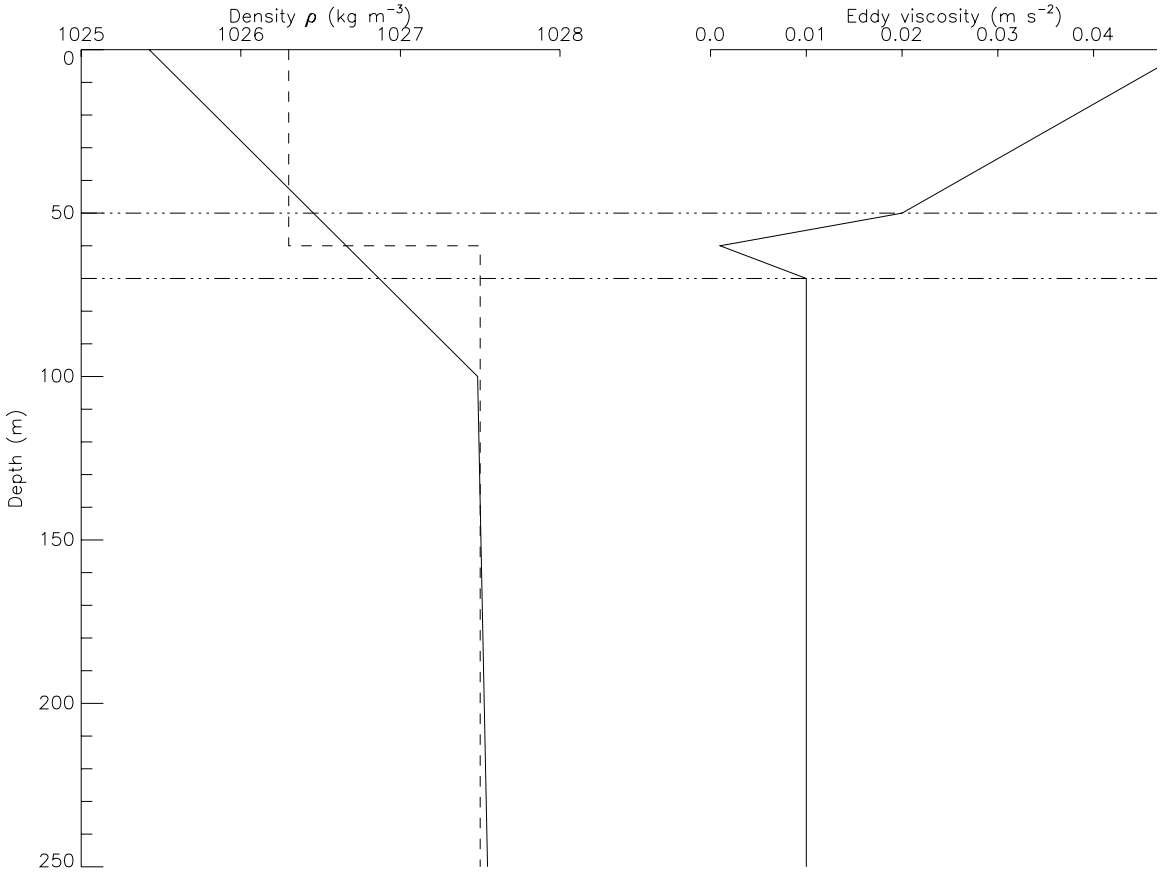

Fig. 1. Profiles of (a) initial density, (b) assumed (specified) eddy viscosity profile.

Calc	**Grid**	**Vertical viscosity**	**Smagorinsky**
BM	64 m (uniform)	A_V	No
1A(B)	G1	A_V	No
2A(B)	G2	A_V	No
3A(B)	G3	A_V	No
4A(B)	G1	0.1 A_V	No
5A(B)	G2	0.1 A_V	No
6A(B)	G3	0.1 A_V	No
7A(B)	G1	tke	No
8A(B)	G2	tke	No
9A(B)	G3	tke	No
10	G6	0.1 A_V	No
11	G1	0.1 A_V	Yes (C=0.2)
12	G6	0.1 A_V	Yes (C=0.2)
13	G6	0.1 A_V	Yes (C=0.002)

Note Where A is higher A_m value and B lower A_m

Table 1
Summary of parameters used in the uniform grid calculations.

the coastal boundary. The reason for the westward propagation is considered later. At the western end of the basin, upwelling of colder (heavier) water (see temperature contours in Fig. 2) leads to some convective mixing, and horizontal temperature gradient (albeit weaker than at the other end) which propagates away from the coastal boundary.

After 40 h (Fig. 2, t=40 h) the temperature front and associated downwelling generated at the eastern boundary has now propagated about 100 km to the west (namely to x=300 km, Fig. 2, t=40 h). Similarly on the western side of the basin, the front that was evident at 20 h (Fig. 2) has now propagated to about x=100 km. However, limited convective mixing has weakened it compared to that at the eastern end.

The lateral speed of propagation of these two fronts appears to be determined by the first internal mode period of the basin. Although, the initial response of the basin is the excitation of all horizontal modes, the first internal mode is the largest and has a period T_1=317 h. This is associated with a speed of propagation of the internal wave (C_i=2.53 km h^{-1}). Hence after 40 h, based on the two–layer analytical model, the temperature disturbance generated at the lateral boundaries has propagated 101 km. The close agreement in the model suggests that the TVD method propagates the disturbance at the correct speed. In addition, as shown by Xing and Davies (1998), the TVD method also retains the sharp temperature gradient associated with the front.

It is important to note that the wind–forced surface current in the region of the eastern boundary is opposed by the current that gives rise to the westward propagation of the density front, leading to a reduction in surface current, and downwelling at the temperature front. Since the magnitude and depth of penetration of this wind–forced current depends upon the value of A_v, then this parameter will influence the intensity of the downwelling in the temperature

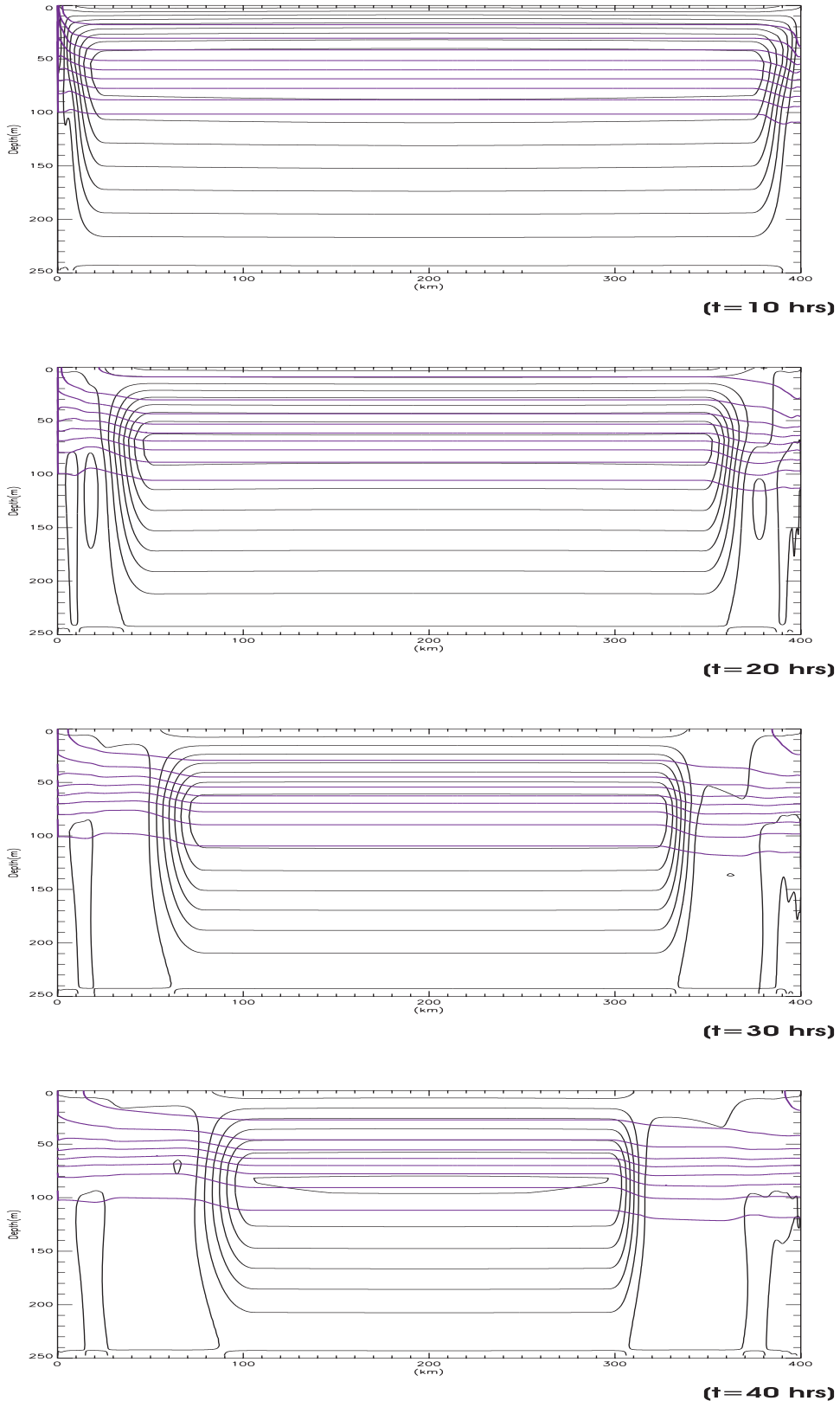

(a)

Fig. 2. Temperature contours (blue) and stream functions (black) over the whole basin at t=10, 20, 30, 40 h and t=80, 160 and 320 h, computed with the benchmark calculation BM (Table 1)

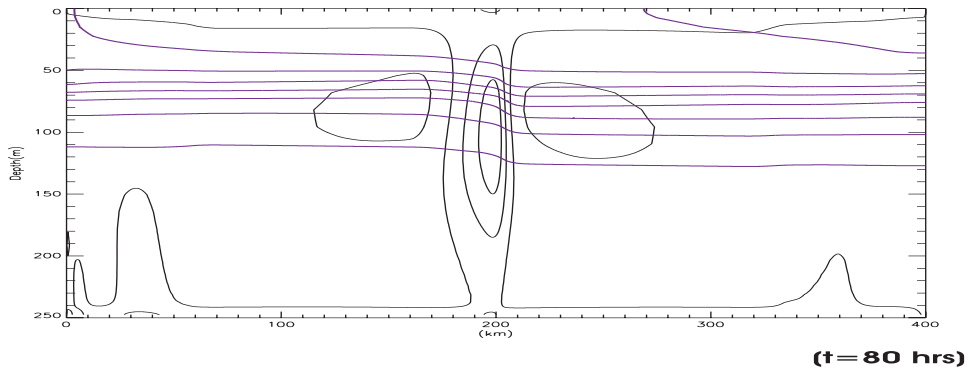
Depth(m)
0
50
100
150
200
250
0
100
200
300
400
(km)
(t=80 hrs)

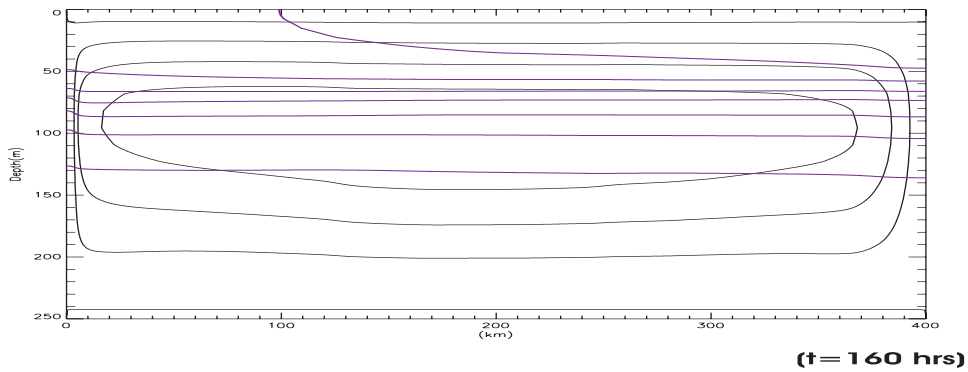
Depth(m)
0
50
100
150
200
250
0
100
200
300
400
(km)
(t=160 hrs)

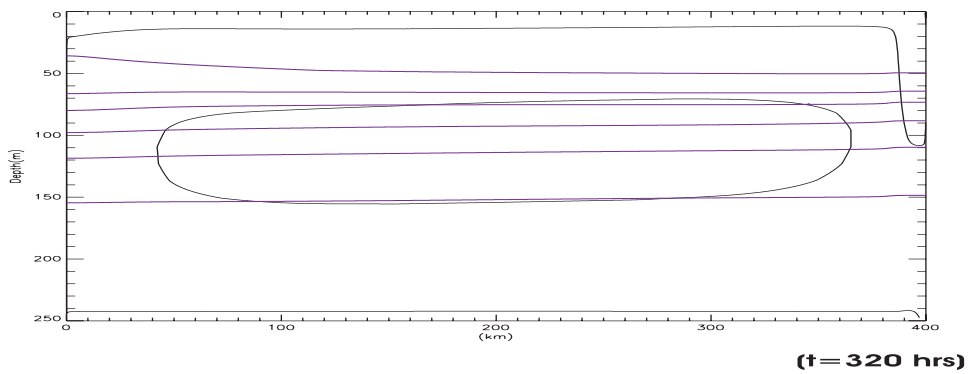
Depth(m)
0
50
100
150
200
250
0
100
200
300
400
(km)
(t=320 hrs)

(b)

Fig. 2. (Contd.)

front. This point will be considered later.

On the western side of the basin, the upwelling in the frontal region, with a surface flow to the west opposes the wind–forced surface current and gives a local downwelling at the western boundary at t=20 h which gradually propagates to the east. This second temperature front produced at t=20 h, due to a local coastal downwelling, has propagated about 25 km from the western boundary by t=40 h. It is evident from Fig. 2 that since there is no convective mixing associated with a temperature front produced by downwelling, these fronts are much sharper, than those produced by upwelling.

As time progresses, the two initial (formed by the sudden wind forcing) frontal systems propagate to the centre of the basin by t=80 h (Fig. 2). This is in close agreement to the time predicted by the speed of propagation based on the analytical model. At this time the temperature surfaces in the eastern half of the basin are almost horizontal, as expected at $t = \frac{1}{4}T_1$ (i.e. approximately 80 h). Wind–induced mixing at the surface and downwelling on the eastern side of the basin leads to a well–mixed surface layer giving a sharper thermocline at about 50 m below the surface (compare Fig. 2, at t=0 and 80 h). The upwelling nature of the flow on the west side of the basin and its surface advection after the windmixing period, leads to a surface temperature front which moves to the east. However by t=160 h, halfway through the internal seiche period, the solution is more anti–symmetrical about the centre of the basin. Mixing below the thermocline increases the mean depth of isotherms in the thermocline region. On the western side of the basin, convective mixing produced by upwelling leads to a loss of the anti–symmetry predicted by the simple linear–layered model.

As time progresses, internal seiche motion in the basin produces downwelling at the western end, with corresponding upwelling at the eastern end, giving rise to nearly horizontal temperature surfaces at t=160 h. Since both ends of the basin have experienced upwelling and downwelling periods by this time, the solution exhibits anti–symmetrical features about the centre (Fig. 2). After 160 h the higher modes have been substantially damped, and the first internal mode corresponding to a linear anti–symmetric vertical displacement of temperature surfaces, about a zero displacement in the centre of the basin remains.

The damping of the higher modes which are responsible for the initial coastal boundary layers can be seen in the across basin variation with time of the temperature at about 90 m below the surface (Fig. 3). It is evident that at t=40 h there is significant spatial variability in the boundary layers due to contributions from the higher modes. Downwelling at the eastern end increases the temperature at 90 m below the surface (Fig. 3) and above its initial condition (about 9.1°C, that occurs in the centre of the basin) due to the downwelling of warmer surface water. At the western side, upwelling moves colder bottom water up to 90 m, producing a reduction in temperature. The differences in the temperature structure in these two boundary layers

Grid	**Resolution (km)**
G1	0.2 (uniform)
G2	2.0 (uniform)
G3	20.0 (uniform)
G4	2.0–20.0 (variable)
G5	0.2–12.3 (variable)
G6	0.2-3.25 (variable)

Table 2
Details of the various grid resolutions.

is due to convective mixing at the upwelling side. As time progresses, the horizontal modes are damped and a more linear across basin temperature variation occurs (t=160 h) which then oscillates at about the period of the first internal seiche. The presence of vertical mixing in the model means that wind–induced temperature gradients give rise to enhanced vertical mixing leading to a reduction by t=320 h of the temperature gradients. Also at a depth of 90 m, the downward mixing of temperature due to wind–forced diffusion leads to an increase in temperature (Fig. 3) as the warmer surface water is mixed to depth.

This "benchmark" calculation clearly shows that horizontal resolution will be particularly important in the coastal regions on the short time scale when higher horizontal modes are present. The influence of viscosity upon these boundary layers and hence grid resolution will be investigated in the next section.

4.2. *Influence of vertical and horizontal eddy viscosity and grid resolution upon the solution*

To examine the effect of changes in horizontal and vertical eddy viscosity together with grid resolution, calculations are performed with a range of uniform grids G1, G2, G3 with resolutions of 0.2, 2, and 20 km (Table 2) and subsequently with a refined grid in the boundary layer ranging from 2 (nearshore) to 20 km (offshore) (G4), from 0.2 (nearshore) to 12.3 km (offshore) (G5), and finally 0.2 (nearshore) to 3.25 km (offshore) (G6). This grid refinement was achieved using a coordinate transformation whereby the grid gradually varied with distance from the coast, rather than grid meshing which involves a sudden change in grid resolution. The gradual grid refinement was incorporated in the model by using a mapping technique in the hydrodynamic equations. By this means finite differencing was still performed on a uniform grid which represented a telescoping grid in physical space. Calculations (Table 1) were initially performed using the eddy viscosity profile and values (A_v) assumed by Davies (1980), although subsequently these values were reduced to 0.1 A_v (Table 1). The influence upon the solution of reducing horizontal eddy viscosity from a value A_M=100 to 10 m^2 s^{-1} was also considered (Table 1, where A denotes calculation with higher viscosity and B with lower viscosity).

As discussed previously in terms of the "benchmark" calculation, the initial response is at the coast, with the coastal boundary layer gradually propagating towards the centre

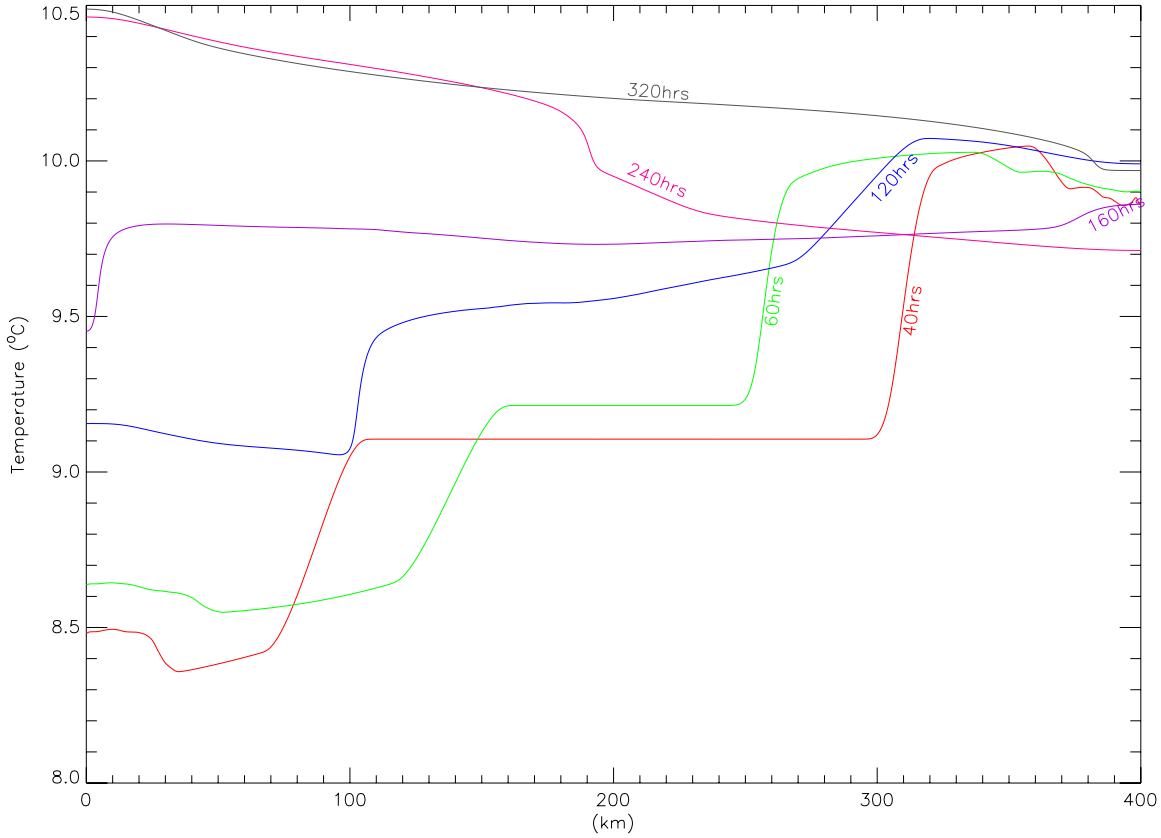

Fig. 3. Contours of temperature at 90 m below the surface at t=40, 60, 120, 160, 240 and 320 h for the benchmark calculation BM (Table 1)

of the basin. This is associated with a region of significant vertical velocity and strong horizontal gradient in the u component of current. To gain some insight into the influence of grid resolution and viscosity upon the solution, we will examine the spatial variability of the current at t=40 h, when the boundary layer has propagated 100 km from the coast (Figs. 4, 5).

A cross–sectional plot of stream function, velocity vectors and temperature (Fig. 4a(1)) from Calc 1A shows the characteristic up– and downwelling regions at 100 km from the coast, caused by a combination of the surface wind–driven flow and internal–wave propagation from the coastal boundary, as discussed previously. The solution with a 2.0 km grid (Calc. 2A) is not substantially different from that with a 0.2 km grid (compare Fig. 4a(1) and (2)) (Calc. 1A). However, with a 20 km grid (Calc. 3A), the region of downwelling vertical velocity at x=300 km is too wide, and the upwelling region is not adequately resolved (compare Fig. 4a(1) and (3)).

When the horizontal eddy viscosity is reduced (Calc. 1B), the circulation computed with the 0.2 km grid (not shown) was not substantially different to that determined in Calc. 1A. Similarly, when a 2.0 km or 20 km grid was used there was no substantial difference from those found with the higher value of A_M. In essence the solution was more sensitive to the grid resolution than to the value of A_M. This can be understood in terms of the generation processes which produce the horizontal gradient in u and the associated vertical velocity. Since grid resolution in the lateral boundary layer has the major effect upon the magnitude of w and hence the gradient in u is clearly of primary importance. As the gradient in u evolves with time it is smoothed by the horizontal viscosity term. However, for the parameters used here the calculations show that the 0.2 or 2 km grid can adequately resolve this gradient which is not particularly sharp and hence not influenced to a large extent by A_M.

In a subsequent series of calculations, (Calcs. 4, 5, 6) A_V was reduced to 0.1 A_V. The effect of this reduction in A_V is an increase in the surface–wind driven current (Calc. 4A, Table 1) in the central part of the basin at t=40 h (Fig. 4b(1)). This leads to an enhanced horizontal gradient in u, and downwelling in the frontal region. A comparable change occurs in the upwelling area, with the general circulation similar to that found with A_V (compare Fig. 4a(1) and b(1)). Similar to the previous one, increasing the horizontal resolution to 2 km gave a comparable flow field (not shown), although with a 20 km grid the spatial distribution changed significantly (compare Fig. 4b(1) and (2)).

A decrease in horizontal viscosity in the 0.2 km grid calculation (Calc. 4B) produced no significant difference in the circulation (not shown) compared to that found previously (Fig. 4b(1)). However, on the 2 km grid (Calc. 5B), at the upwelling end, two small gyres appeared in the vertical which were not present in previous calculations (compare Fig. 4b(1) and (3)). These gyres appear to arise due to a

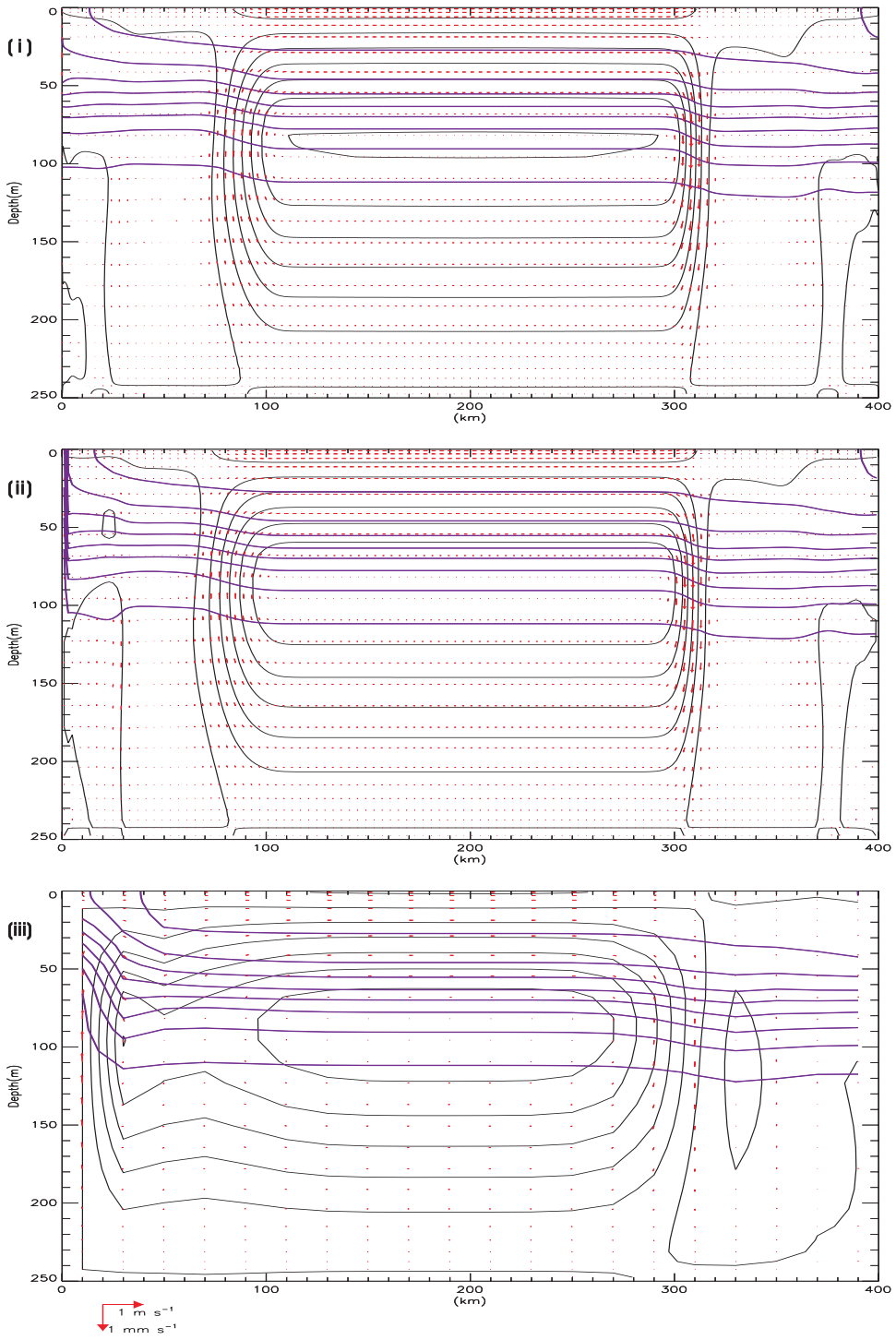

(a)

Fig. 4. Stream function (black) and temperature (blue) contours at t=40 h together with velocity vectors (sampled at every 5 km) (vertical velocity scaled by 103) for a(1) Calc. 1A, (2) Calc. 2A, (3) Calc. 3A b(1) Calc. 4A, (2) Calc. 6A, (3) Calc. 5B c(1) Calc. 7A, (2) Calc. 8A, (3) Calc. 9A d(1) Calc. 7B, (2) Calc. 8B, (3) Calc. 9B

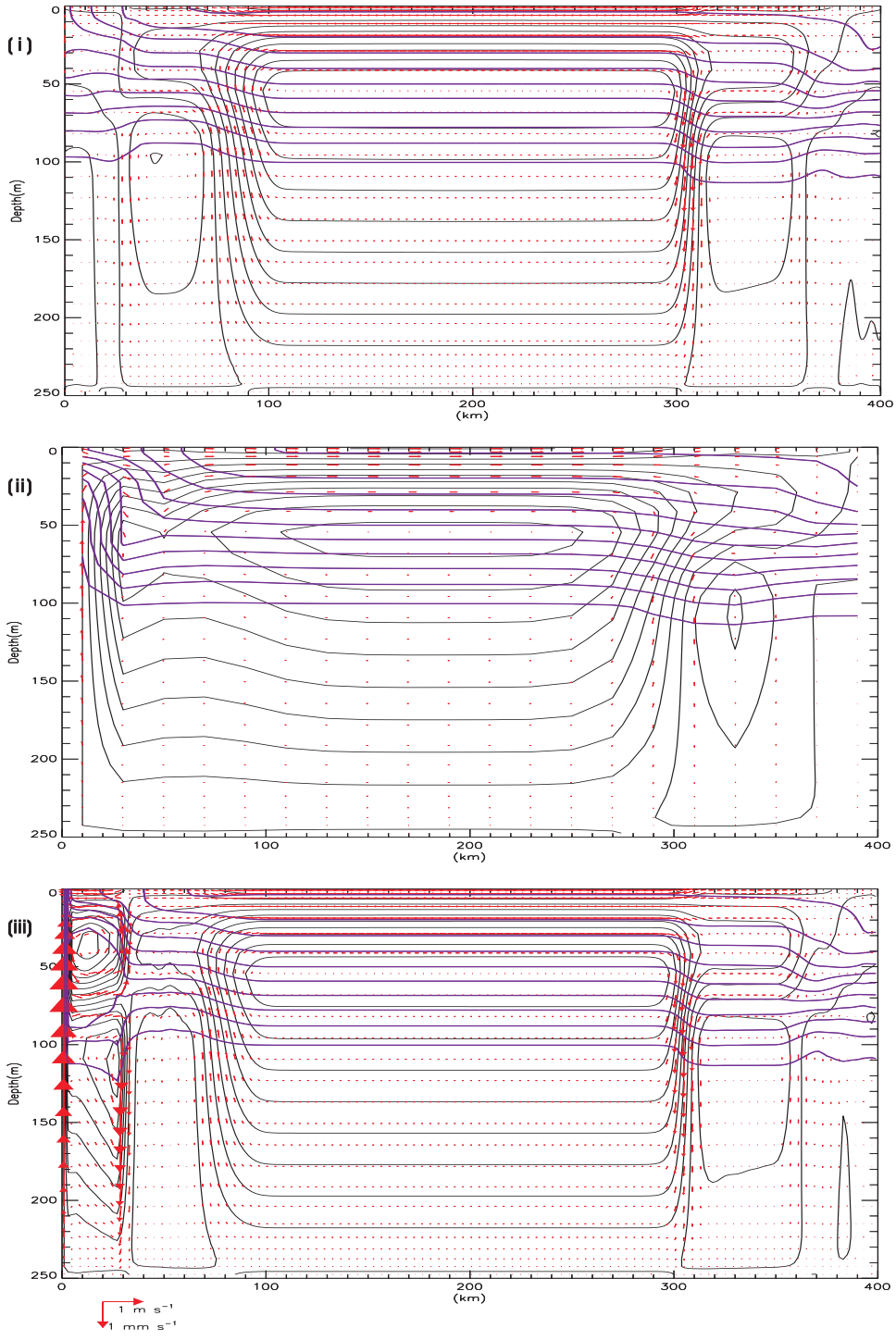
(i)
(ii)
(iii)
Depth (m)
(km)
0
50
100
150
200
250
0
100
200
300
400
1 m s⁻¹
1 mm s⁻¹

(b)

Fig. 4. (Contd.)

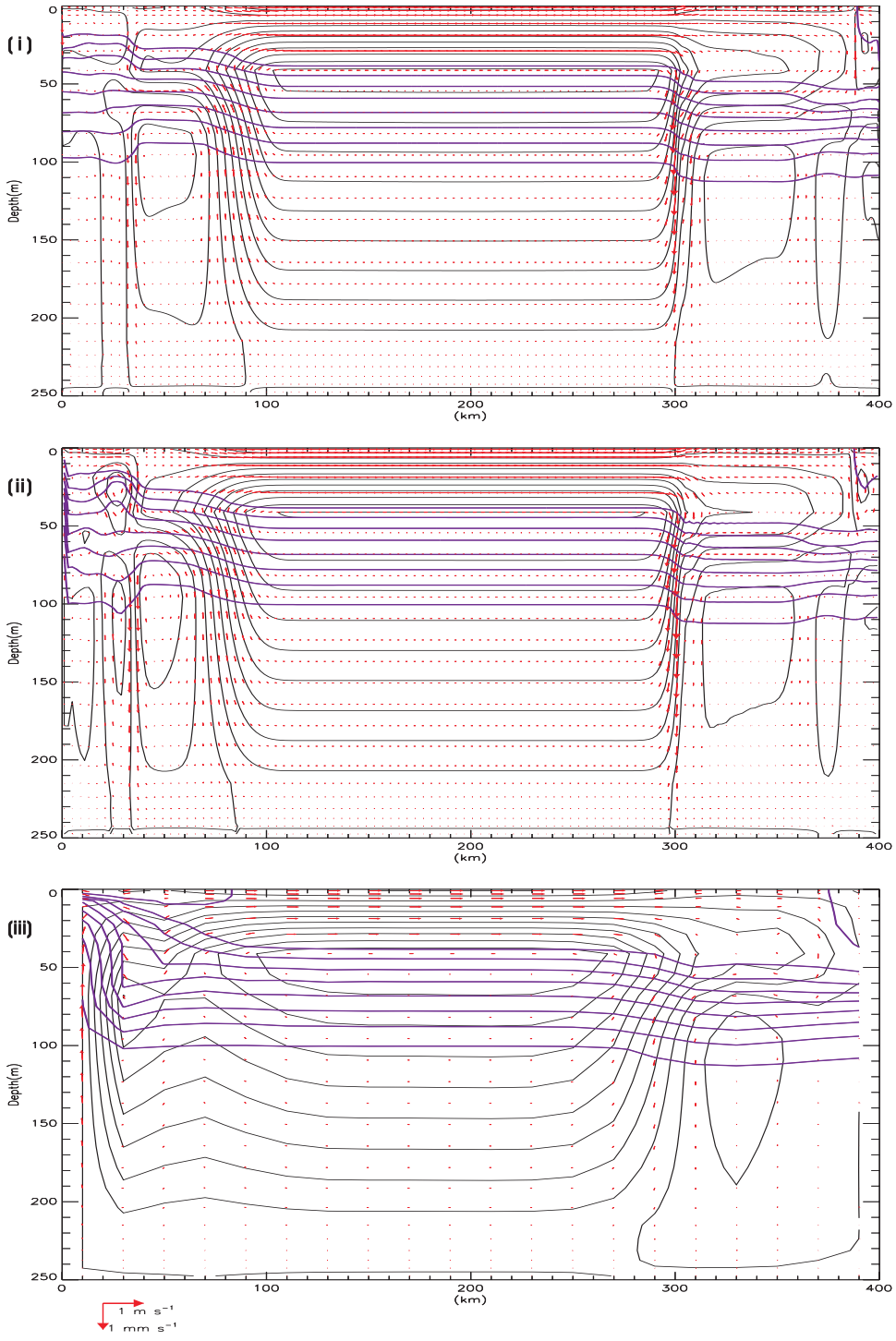
(i)
(ii)
(iii)
Depth(m)
0
50
100
150
200
250
0
100
200
300
400
(km)
1 m s⁻¹
1 mm s⁻¹

(c)

Fig. 4. (Contd.)

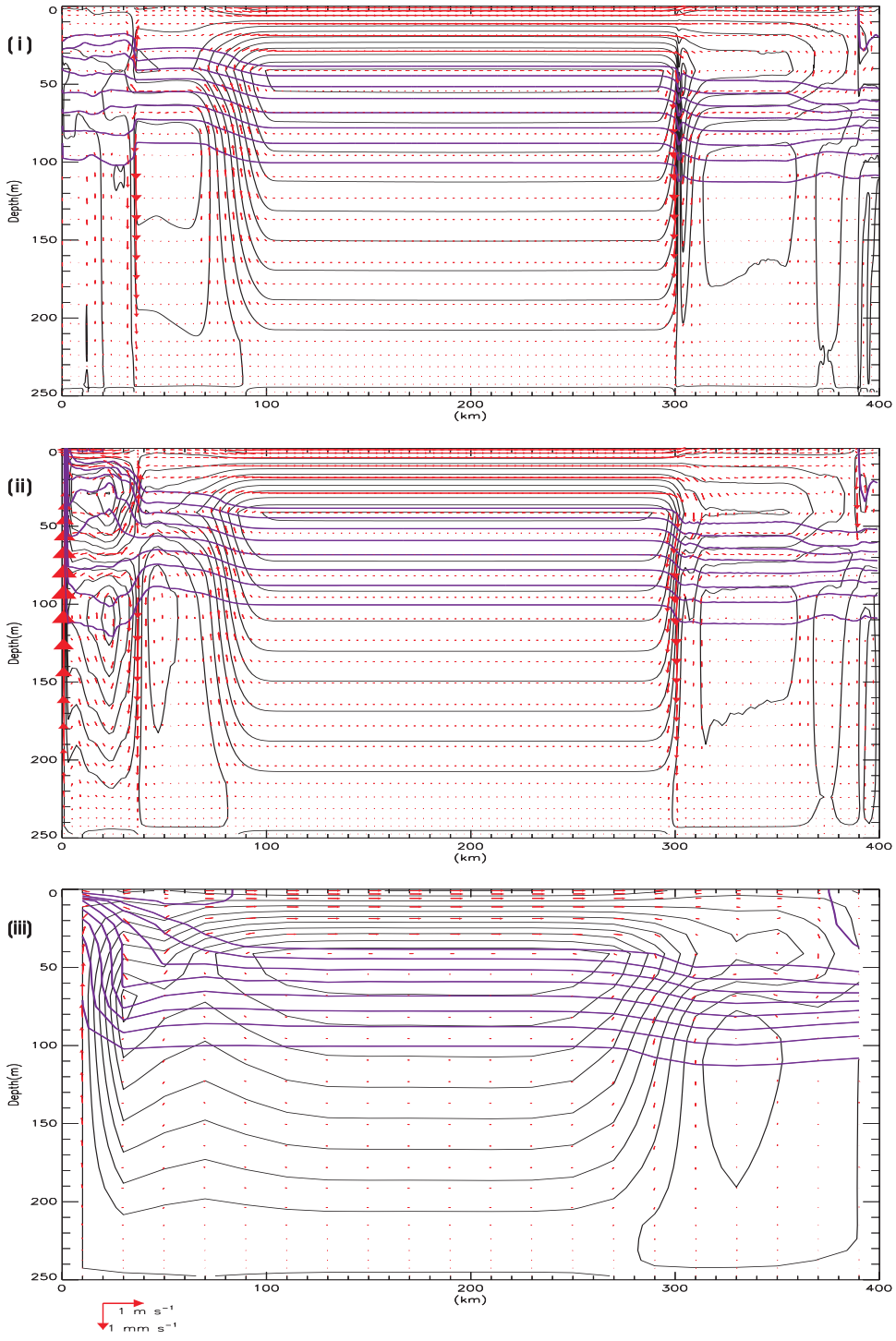
(i)
(ii)
(iii)
Depth(m)
(km)
0
50
100
150
200
250
0
100
200
300
400
1 m s⁻¹
1 mm s⁻¹

(d)

Fig. 4. (Contd.)

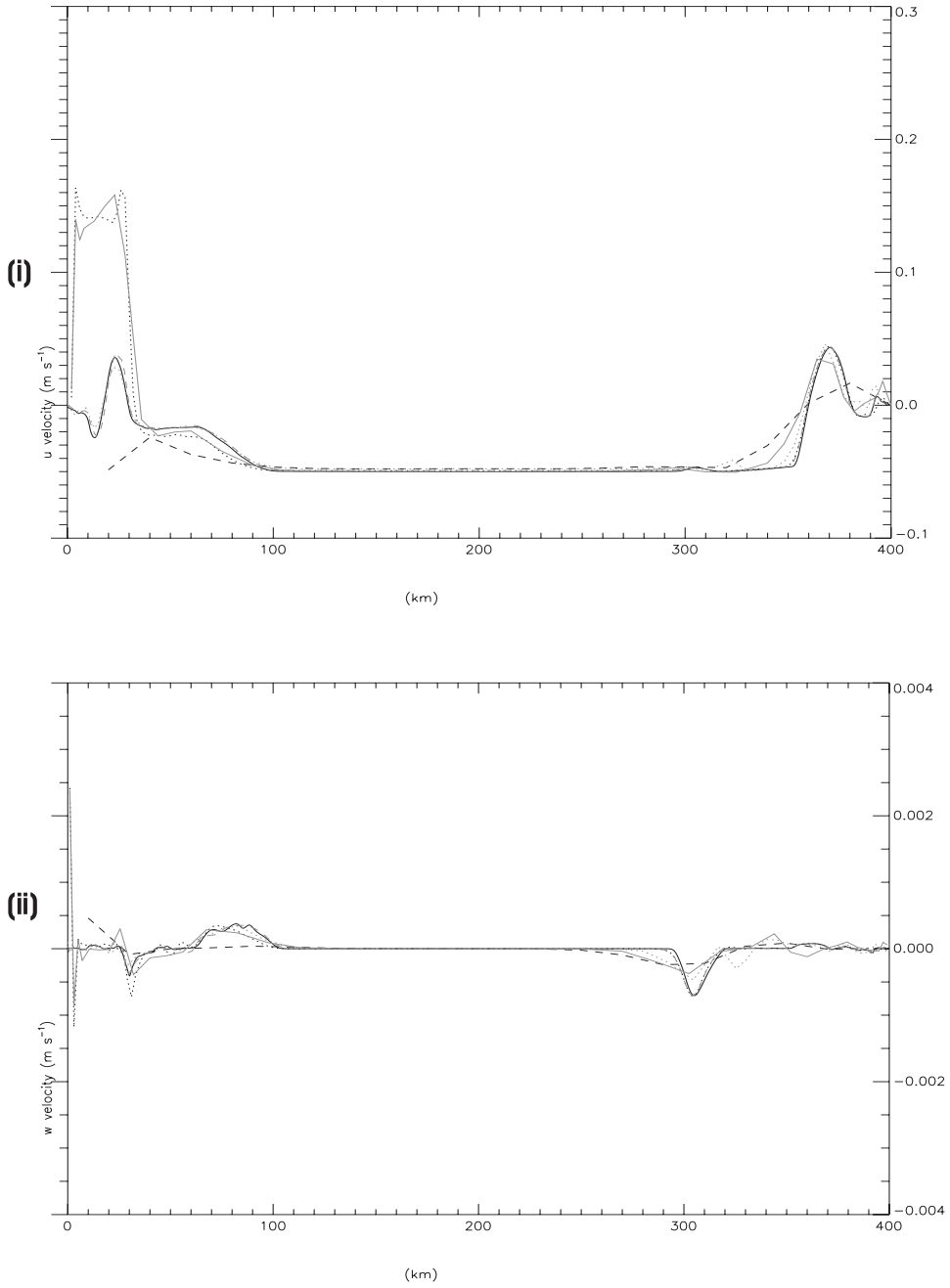

(a)

Fig. 5. (a) Across basin plot of (1) u current, and (2) w current, and (b) limited area (100 km) enhanced resolution plot using compressed scale close to western coastal boundary of (1) u and (2) w current velocity. For grid G1 (black solid line), G2 (black dotted), G3 (black dashed), G4 (grey solid), G5 (grey dotted) and G6 (grey dashed), using eddy viscosity values of 0.1 A_V and A_m=10 m^2 s^{-1} (low horizontal viscosity). (c), (d) As Fig. 5a and b but with eddy viscosity computed using the turbulence energy model and A_m=10 m^2 s^{-1} (low horizontal viscosity)

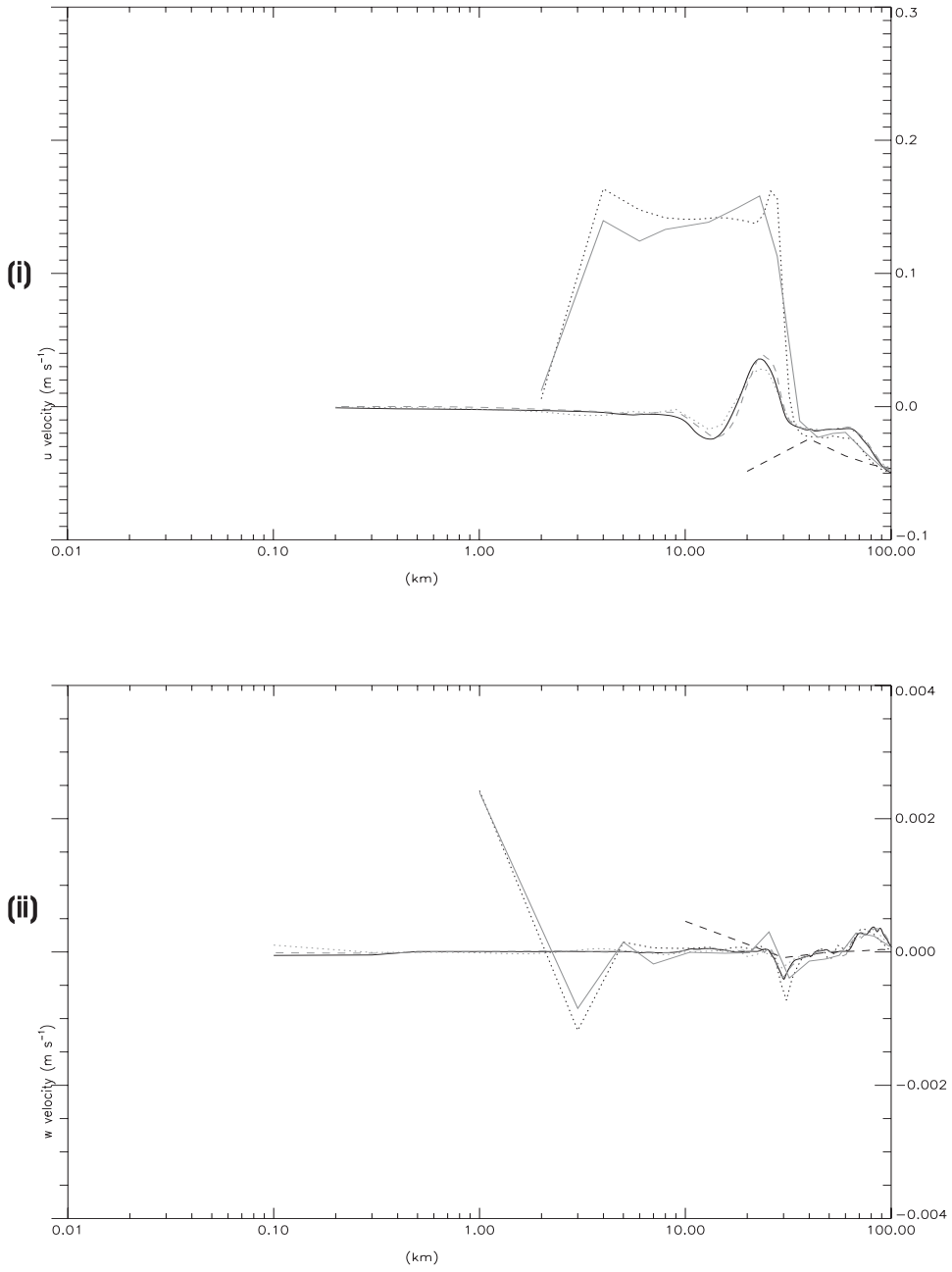

(b)

Fig. 5. (Contd.)

down–wind flow at the level of the thermocline, which at about 30 km from the coastline produced an upwelling and downwelling flow. Some indication of a comparable flow is evident at the downwelling end at about 3040 km from the coast although it is less pronounced. This circulation appears to be a function of the value of A_M and the grid resolution, in that there is no evidence for it in Fig. 4b(1). With a 20 km grid resolution, the circulation (not shown) was not substantially different from that given in Fig. 4b(1).

To consider the effects of variable grid resolution in detail, we will consider the case where vertical viscosity is 0.1 A_V and horizontal viscosity is low at A_M=10 m^2 s^{-1}. At t=40 h, a cross basin plot of horizontal and vertical velocity at 90 m below the surface shows the gradient in horizontal velocity and the rapid increase in vertical velocity (Fig. 5a(1)) for a range of grids. A depth of 90 m below the surface was chosen as this is the region of the thermocline where vertical velocity is a maximum. Increasing the horizontal grid resolution widens the coastal boundary layer which shows less spatial variability as the model does not have sufficient resolution to adequately resolve the region of rapid change.

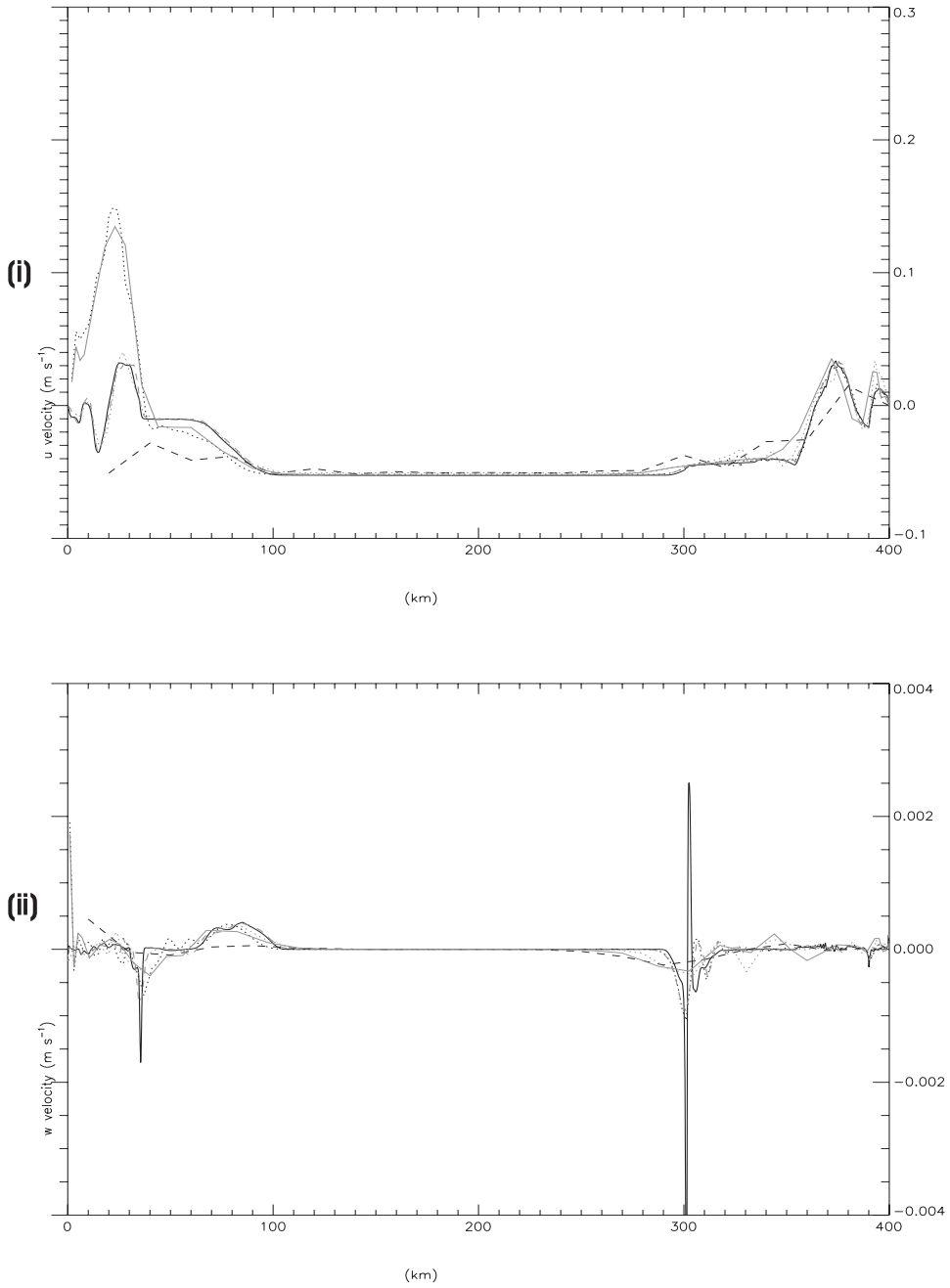

(c)

Fig. 5. (Contd.)

This is evident in the cross basin variation of the u current determined with the uniform 2 km grid (G2) or variable grid (G5) which shows an artificial (compared with grids G1 or G6) variation close to the western coastal boundary. This appears to be associated with the two vertical gyres discussed previously. In the case of the coarse grid (20 km), the model cannot resolve the spatial variability of u current that occurs in the lateral boundary layer. The vertical velocity w computed with the fine grid (G1) on the eastern side of the basin has a region of rapid change which is well resolved on the 0.2 km grid (G1), or on the variable resolution grids (G5 and G6). With the G4, G5 and G3 grids where the resolution is too coarse, there are major errors.

Expanded versions of Fig. 5a(1) and (2), at the western side of the basin, namely, Fig. 5b(1) and (2), clearly show that grids G1, G5 and G6 give comparable solutions. However, G2 and G4 which use a 2 km grid in the boundary layer are significantly different from the others. This suggests that a variable resolution grid with order 0.2 km in the coastal region may yield an accurate solution.

The sensitivity of the solution to the horizontal grid resolution is clearly evident from these calculations. For a

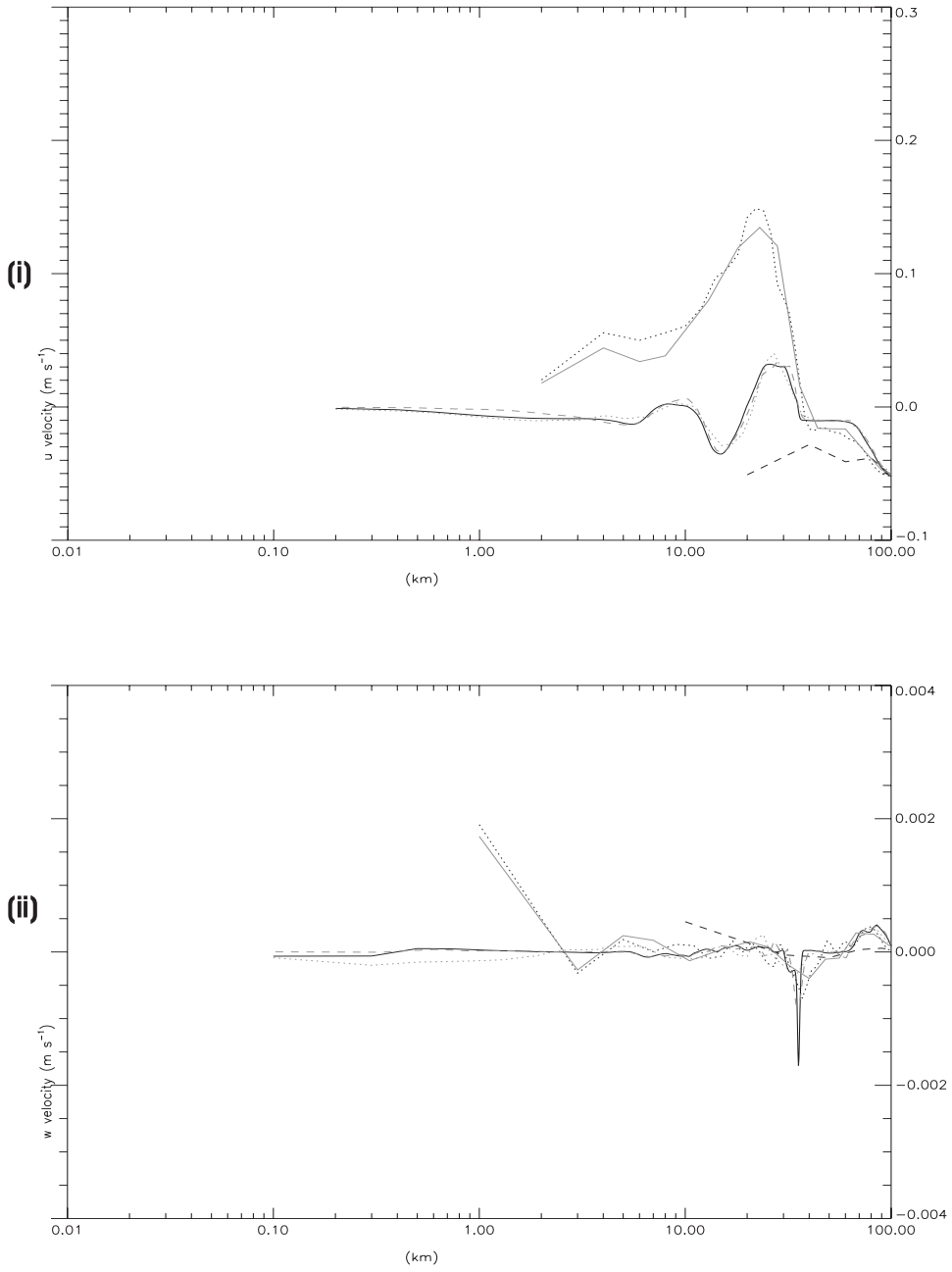

(d)

Fig. 5. (Contd.)

given grid resolution, as the value of vertical eddy viscosity is reduced the surface current increases giving enhanced up– and downwelling in the lateral boundary layers, and a sharper horizontal gradient in u and w. This suggests that as the surface eddy viscosity is reduced, then the horizontal gradient in u, and hence the vertical velocity associated with it will increase; provided that the grid in the near coastal boundary layer is sufficiently fine to resolve these features. If the grid is too coarse in this lateral boundary layer, then this important physical process will not be resolved.

4.3. *Calculations using a turbulence energy model to compute A_V and K_V*

In an initial calculation (Calc. 7A, Table 1) the turbulence energy model was used to compute the profile of vertical eddy viscosity. As the mixing length in the model decreased to a small value in the surface layer, the eddy viscosity profile exhibited a small surface value, increasing with distance below the surface to a value comparable to that used in the fixed viscosity calculations. At the level of the thermocline it fell to near zero due to the suppres-

sion of turbulence by stable stratification. Below this level, except in the near bed region, shear was small, and hence turbulence production and eddy viscosity were negligible.

The effect upon the surface current of the small surface value of eddy viscosity is to appreciably increase the surface current (Fig. 4c(1)) compared to the one discussed previously (Fig. 4a(1), b(1)), with an associated increase in u current gradient and downwelling velocity. A similar although less dramatic increase in upwelling also occurs, although the main features of the circulations are comparable (compare Fig. 4b(1) and c(1)). An increase in grid resolution to 2 km (Calc 8A) (Fig. 4c(2)), although producing only a small change at the eastern end, does affect the flow at the western end of the basin. With a coarse grid (Calc. 9A), the regions of strong vertical velocity are removed (Fig. 4c(3)).

A reduction in horizontal viscosity (Calc. 7B), with a fine horizontal grid (G1, Table 1), leads to a significant increase in u current gradient and vertical velocity which shows the presence of a small internal shock on the density surfaces (Fig. 4d(1)). As discussed previously, as the horizontal grid is increased (Calc 8B) (Fig. 4d(2)) a two gyre system in the vertical develops at the upwelling (western) end of the basin (Fig. 4d(2)). However, at the downwelling end, the internal shock is spread over a larger region with some evidence of small ripples behind the front. As before, a coarse grid (Calc. 9B) leads to a solution which only exhibits the large–scale features of the detailed flow field found with the finer grids.

Cross–sectional plots of u and w velocity at a depth of 90 m below the surface are given in Fig. 5c(1) and (2) for the range of grid resolutions shown in Table 2. These show that at the eastern end of the basin the main features of the u velocity can be represented on all grids except the coarse grid G3. However, as earlier, at the western end, only the 0.2 km uniform grid G1 or variable grid G6 can adequately resolve the region, as shown in the "blow up" figure (Fig. 5d(1)). For the w component of velocity, both the sharp "spike" at the western side of the basin (Fig. 5c(2) and d(2)) and the small horizontal scale with large amplitude variation at the eastern side (Fig. 5c(2)) require a grid resolution of order 0.2 km to adequately resolve them.

These calculations clearly show that as the surface viscosity is reduced, the surface–wind driven flow increases giving rise to a significantly larger downwelling current in the coastal boundary at the eastern end of the basin. If a sufficiently fine grid and low enough horizontal viscosity is used in the calculation, then a sharp horizontal temperature gradient and associated vertical velocity propagates away from the boundary. With a coarse grid or large horizontal viscosity, this feature is removed from the solution. The results suggest that a fine grid in the lateral generation region may be sufficient to produce an accurate solution, since as the analytic solution suggests high order modes are rapidly damped in time.

4.4. *Longer time integration solutions with a variable grid resolution*

4.4.1. *Constant horizontal diffusion coefficient*

The previous series of calculations have shown that as vertical and horizontal viscosity are reduced, resolution within the lateral boundary layers becomes more important on the short time scale. However, as time progresses, small–scale features associated with the initial excitation of higher modes propagate away from these boundary layers into regions where the grid is coarser. As shown in the analytical solution, the damping of these higher modes is larger than for the lower modes and consequently any disturbance that propagates from the lateral boundaries will be damped with time. However, this could be a problem on an irregular grid where propagation into a coarse grid region could lead to a spurious solution if the propagation to the coarse grid region was rapid compared with the damping. This problem is examined in this section.

In calculation 10 (Table 1) grid G6 was used with a low value of Am and viscosity 0.1 Av. Contours of T, u, w at 10–h intervals up to 80 h at 90 m below the surface (Fig. 6a) show a disturbance propagating away from each coastal boundary. Some indication of a Gibbs–type oscillation in the T field following the frontal region, as it propagates into the coarser grid, is apparent, suggesting a lack of resolution in this region. It is evident that the intensity of the ripples particularly on the T contours increases with time (Fig. 6b). Any short waves that are produced on the longer time scale can transfer energy through non–linear effects down to grid scale waves giving rise to an unstable solution.

Additional calculations (not presented) showed that increasing A_m introduced more horizontal smoothing giving a stable solution. This excessive smoothing, however, negated the effects of having an enhanced resolution in the lateral boundary layers. To avoid this problem a grid–dependent horizontal viscosity, namely a Smagorinsky formulation, was examined.

4.4.2. *Smagorinsky formulation of diffusion coefficient*

In an initial calculation (Calc 11) using A_m computed with the Smagorinsky formulation with C=0.2, a uniform grid resolution of 0.2 km was employed. Although on the short time scale up to t=80 h the main features of the T, u, w fields (Fig. 7a) were consistent with those found previously (Fig. 6a), it is apparent that at t=80 h the Gibbs–type effect in the temperature field was not present. Similarly, on the longer time scale there were no spurious oscillations in the T field, even though the spike associated with the vertical velocity was resolved in the solution (Fig. 7b). From a comparison with the benchmark solution (Calc BM) presented earlier (Fig. 3), it is evident that with a fine horizontal grid the Smagorinsky solution is not significantly different (except for a reduction in the peaks in the vertical velocity field) from that found previously with a low value of Am.

To examine to what extent the Smagorinsky formula-

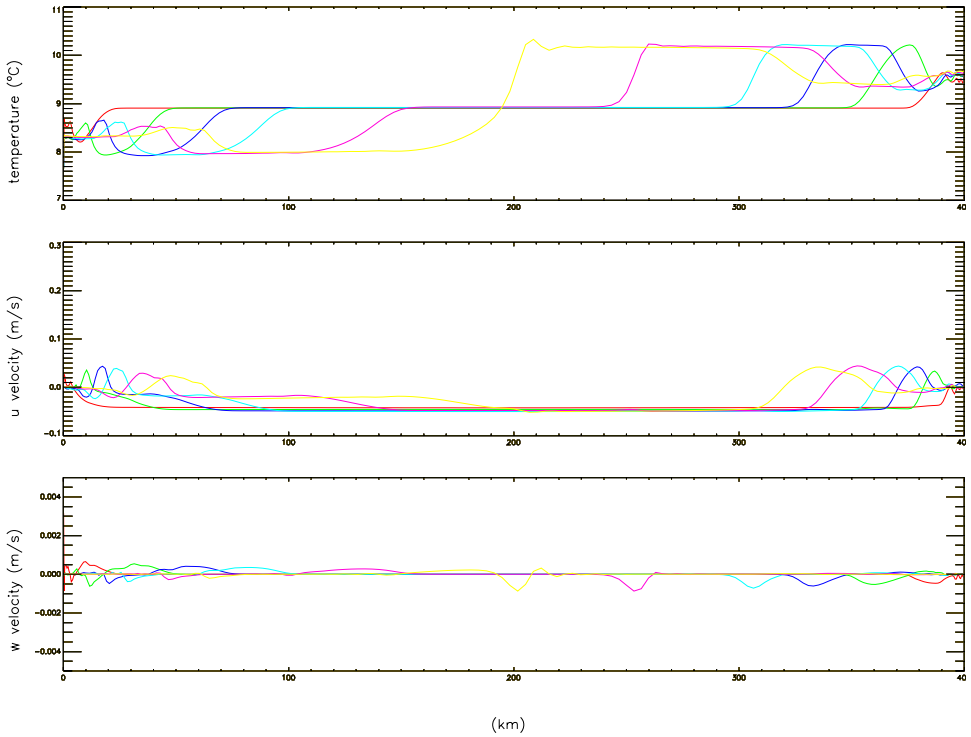

(a)

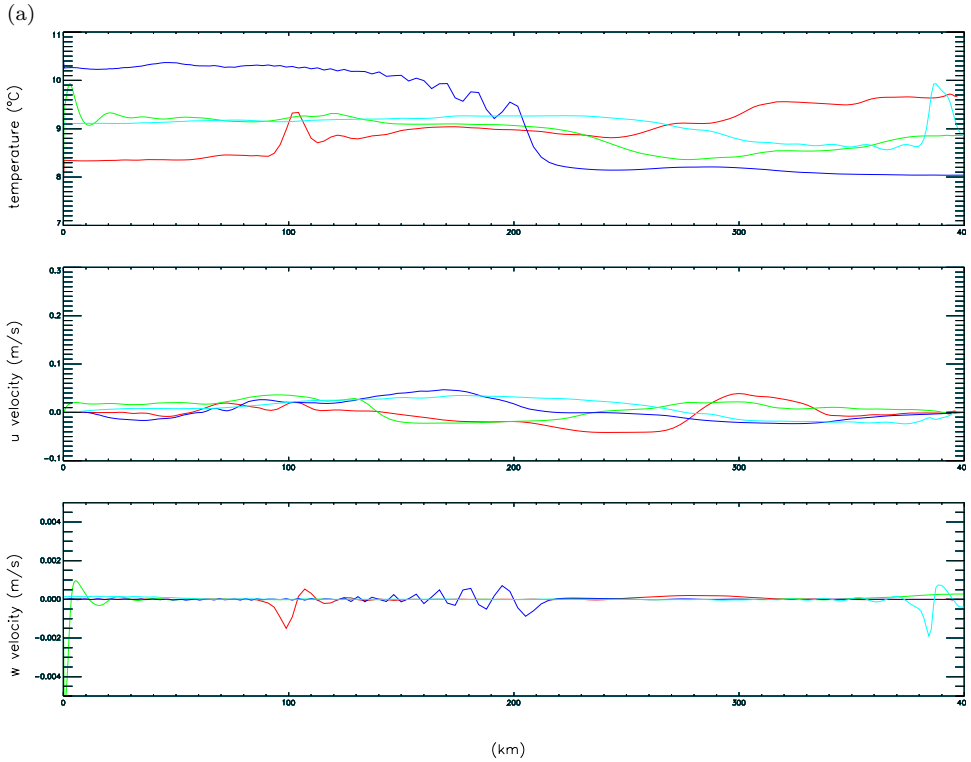

(b)

Fig. 6. Across basin contours of (1) temperature (°C), (2) u velocity (cm s^{-1}), (3) w velocity$\times 10^{-3}$ (cm s^{-1}) at (a) t=10, 20, 30, 40, 60, 80 h and (b) t=120, 160, 240, 320 h. Colours used are red (t=10 h), green (t=20 h), blue (t=30 h), cyan (t=40 h), magenta (t=60 h), yellow (t=80 h), and then red (t=120 h), green (t=160 h), blue (t=240 h) and cyan (t=320 h). Computed with Calc 10 (A_m=10 m^2 s^{-1}, grid G6)

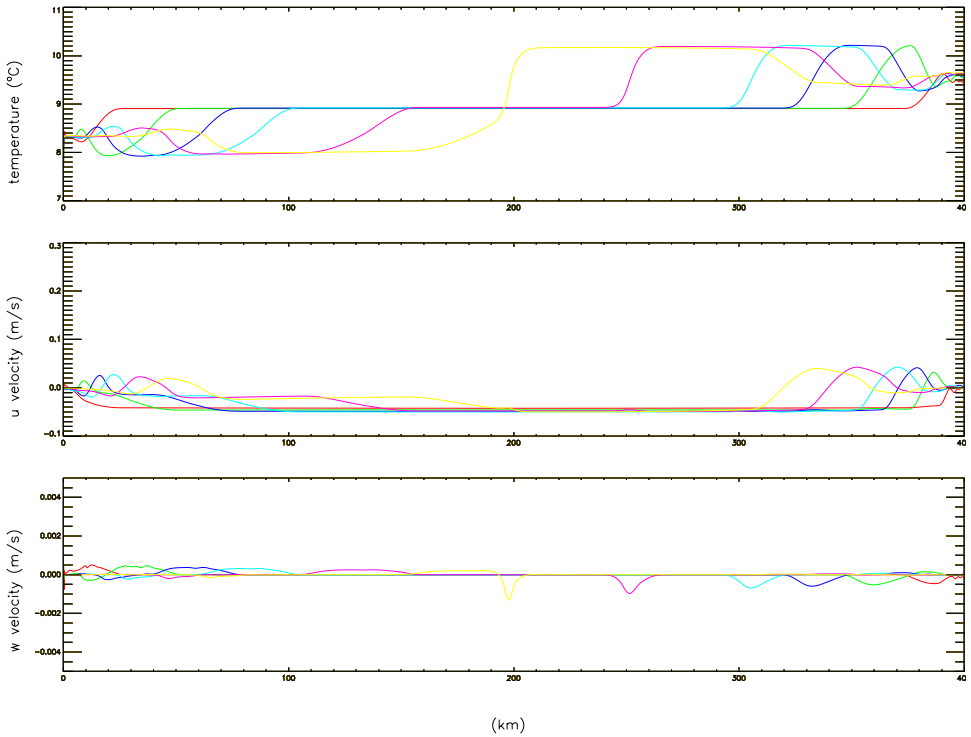

(a)

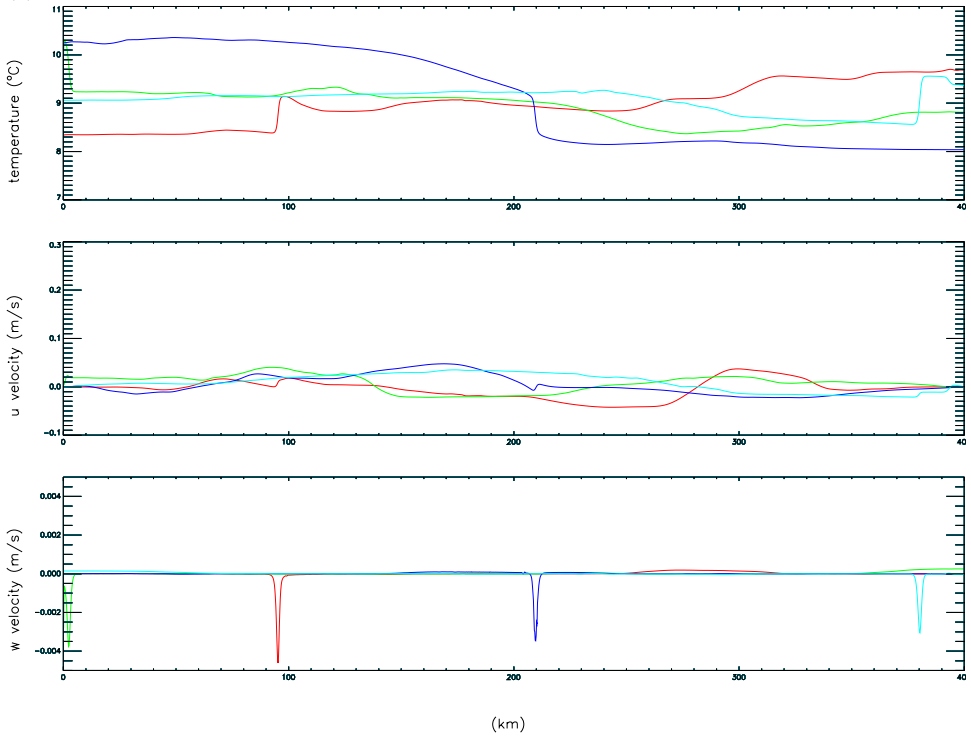

(b)

Fig. 7. As Fig. 6 but for Calc 11 (A_m from the Smagorinsky formulation (C=0.2, grid G1))

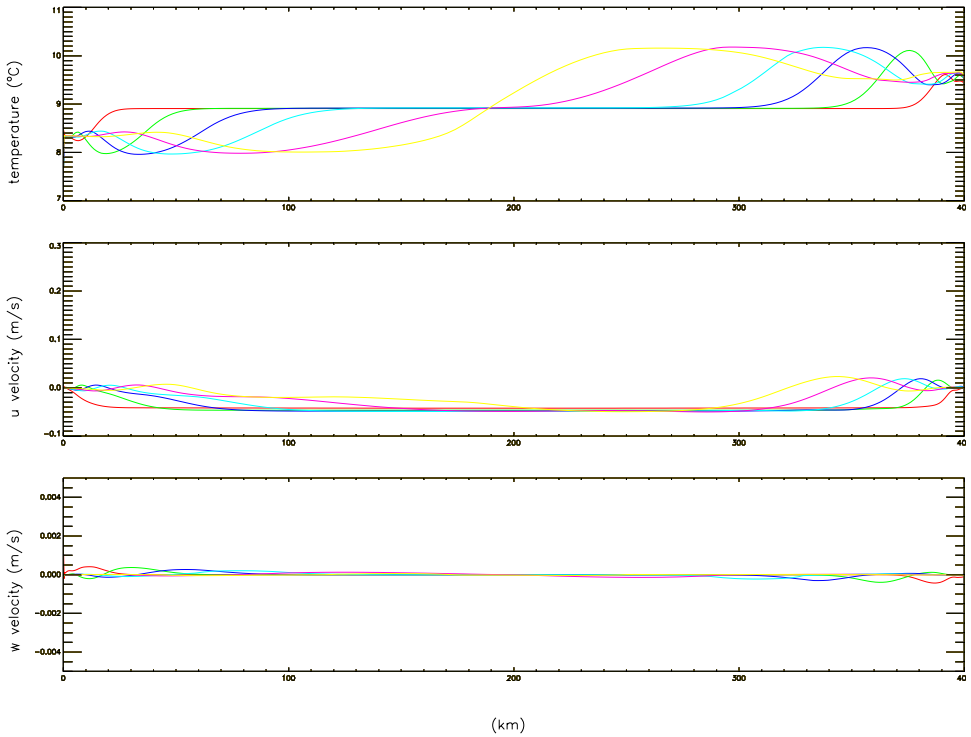

(a)

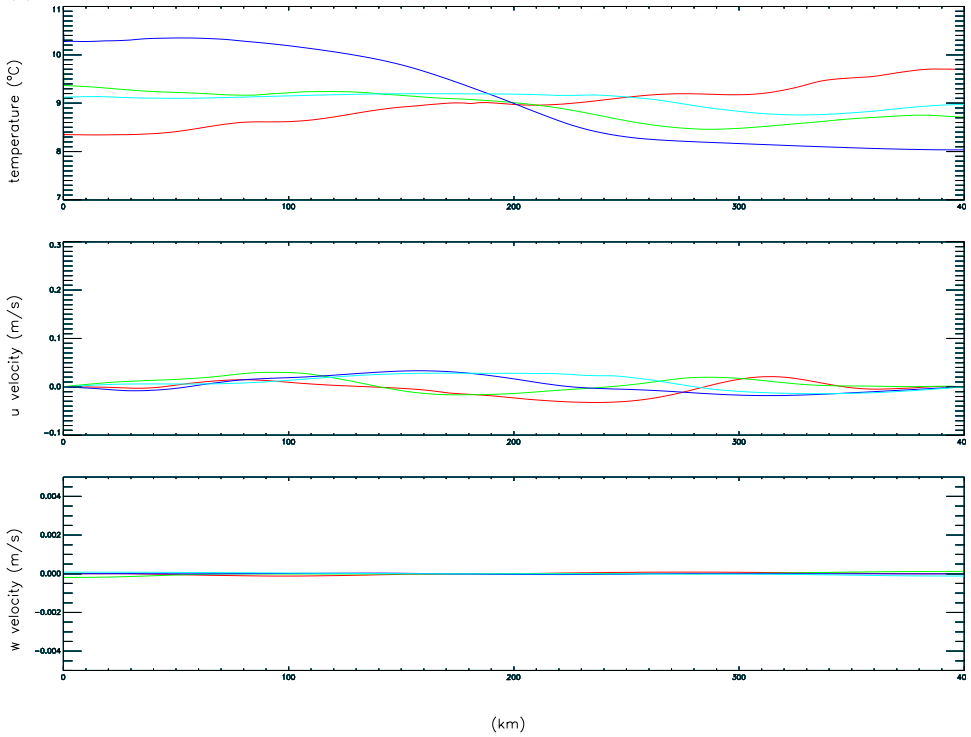

(b)

Fig. 8. As Fig. 6 but for Calc 12 (A_m from the Smagorinsky formulation (C=0.2, grid G6))

tion (with C=0.2) could reproduce the benchmark solution on the irregular grid the previous calculation was repeated with grid G6 (Calc 12). From Fig. 8a it is evident that although on the very short time scale (t¡20 h) the model can reproduce the disturbance coming from the coastal boundary, on the longer time scale t=80 h, excessive horizontal smoothing takes place (compare Fig. 8a with Calc 11 Fig. 7a) as the disturbance reaches the coarser grid. In addition, on the long time scale (t=240 h, Fig. 8b) none of the small scale structure found in Calc (11) is evident in the temperature field. Similarly there are no spikes in the vertical velocity field (Fig. 8b, compared to previously Fig. 7b). This excessive smoothing on the irregular grid using the Smagorinsky formulation with C=0.2 can be attributed to the fact that the computed A_m depends not only on horizontal shear but also on grid scale Δx which increases in the coarse grid region of the model.

Contours of T, u, w computed using the irregular grid (G6) but with C=0.002 (Calc 13) up to t=80 h (Fig. 9a) are in excellent agreement with those found in Calc 11 (Fig. 7a). However, it is apparent that the maximum value of w associated with the disturbance which propagates from the coastal boundary has been reduced. On the longer time scale, the T and u distributions (Fig. 9b) are in good agreement with those found with the high resolution uniform grid (Fig. 7b) although the magnitude of the vertical velocity spikes has been significantly reduced. Unlike previous calculations the use of a Smagorinsky formulation with C=0.002, with an irregular grid, does not introduce excessive smoothing, (hence negating the advantages of an irregular grid) or allow for a build–up of grid scale energy on the coarse grid, leading to a physically unrealistic solution. In essence, when the Smagorinsky formulation for A_m is used on an irregular grid, the value of C is critical in determining the solution. The determination of an optimum value of C will depend upon the degree of mesh refinement in the grid, and will influence the solution.

5. Concluding remarks

The problem of internal–wave seiching in a wide basin has been used to examine the physical processes giving rise to the horizontal propagation of small–scale features from the lateral boundaries into the centre of the basin. Calculations have shown that this problem is ideal for examining the influence of a variable grid upon the accuracy of the solution. By using a constant depth basin without rotational effects and an essentially twolayer density profile, an analytical solution could be obtained which yielded significant insight into the physical processes governing the solution and their role in determining an optimum grid size.

On the short time scale, the numerical solutions showed that the response to a wind pulse was coastally induced downwelling at the downwind end of the basin, and an associated upwelling and convective mixing (in the numerical solution) at the upwind end. This gave rise to an appreciable non–zero vertical velocity close to the coast which gradually propagates into the centre of the basin. By using a long basin the two lateral boundaries were well removed and the horizontal propagation could be studied in detail. Associated with the region of non–zero vertical velocity was a horizontal temperature front.

Calculations using a fine (64 m) horizontal grid showed that the TVD advection scheme in the model could accurately reproduce the lateral advection of this front. However, as the horizontal grid became coarser this front could not be formed in the coastal boundary and the numerical solution departed from the accurate benchmark solution. Also if horizontal eddy viscosity was increased the solution was smoothed in the horizontal.

The intensity of the vertical velocity in the boundary layer and the associated sharpness of the temperature gradient was also found to be sensitive to the value of vertical eddy viscosity. With a low surface value of viscosity, the winds momentum was confined to the surface layer rather than diffusing to depth. This gave an enhanced near surface transport with increased up– and downwelling in the coastal boundary layer and hence a sharper internal temperature front.

Calculations using an irregular finite difference grid, with enhanced resolution in the coastal region and with low values of A_m and A_V, showed that as the temperature front propagated away from the coastal boundary into the coarse grid region, a Gibbs–type effect occurred behind the propagating front. This arose due to a lack of local grid resolution. In addition, on the longer time scale non–linear effects lead to short–wave ripples in the large–scale solution.

Solutions derived with a high resolution (0.2 km) uniform grid with A_m computed using a Smagorinsky formulation with C=0.2 were not significantly different from the "benchmark" solution. However, when a grid transformation was used with the same value of C, significant smoothing occurred as Am was increased in the coarse grid region. This had the effect of negating the benefits of using a finer grid in the boundary layers. A solution with C=0.002 and the irregular grid was, however, in good agreement with the benchmark solution.

These results showed the importance of maintaining a high resolution in the near coastal boundary layers. This has been a common policy adopted in finite element models of shallow seas, where in order to resolve the coastal boundary correctly a high resolution finite element grid was used. However, the calculations also demonstrate that in the case of stratified flows where internal waves generated in offshore, (Davies and Xing 2003; Xing and Davies 2001b,a) or land regions (Davies and Xing 2004) subsequently propagate away from their generation region, as it is essential to maintain adequate grid resolution. In a coarse grid non–linear model, numerical instability can arise unless a scale selective filter is applied. One means of avoiding this is to use the Smagorinsky formulation which takes account of local grid size and horizontal current gradients in determining the value of Am. This approach selectively smooths

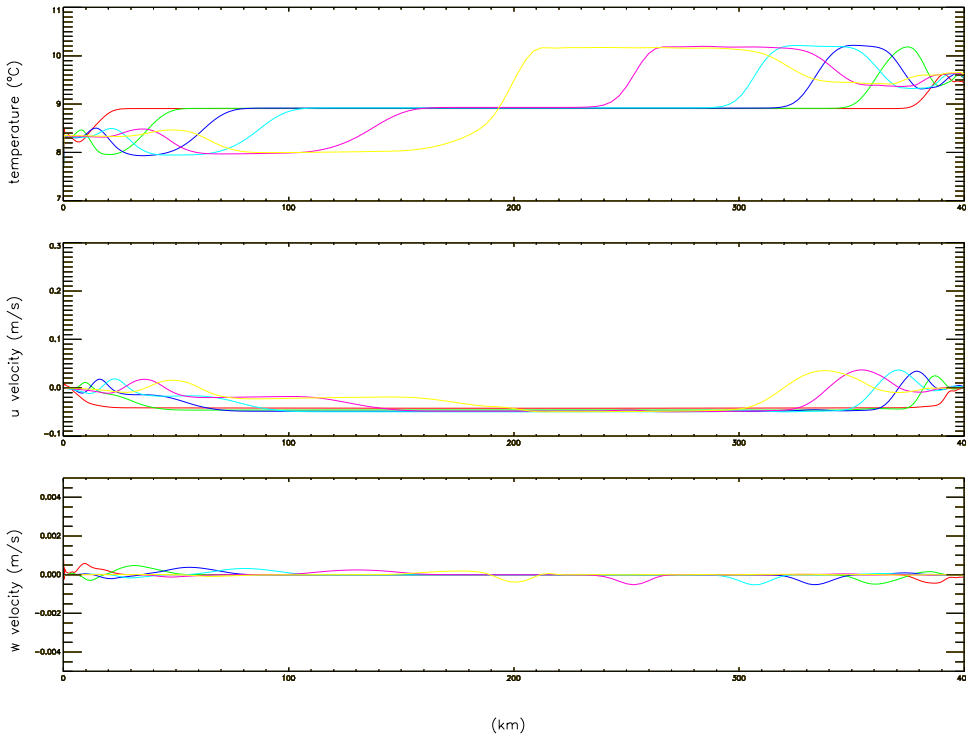

(a)

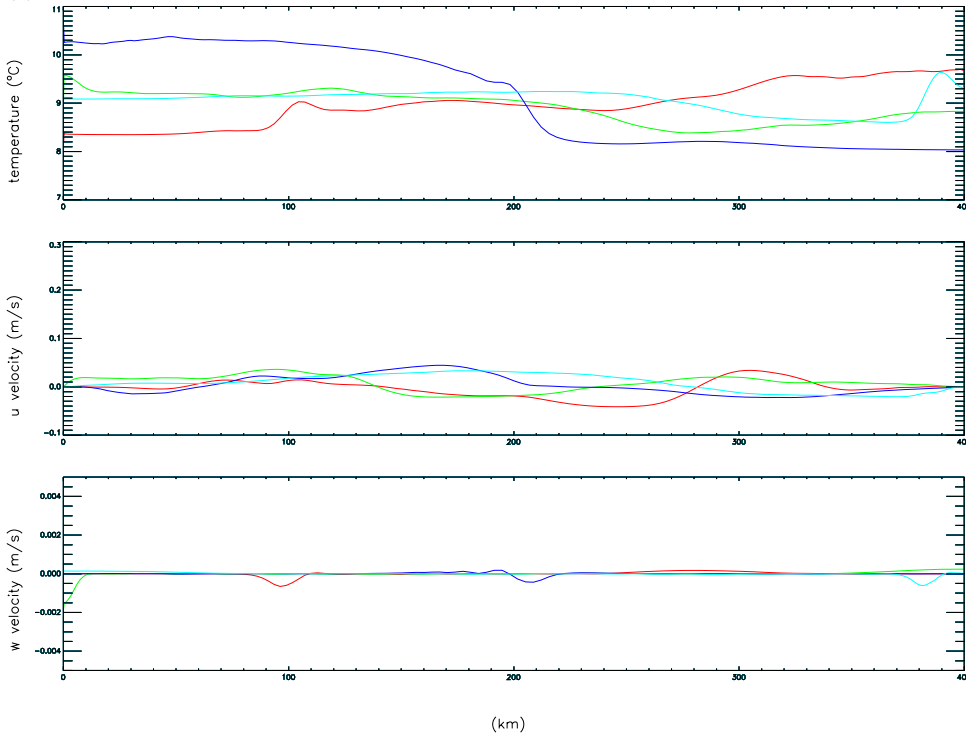

(b)

Fig. 9. As Fig. 6 but for Calc 13 (A_m from the Smagorinsky formulation (C = 0.002, grid G6))

the flow field, although the choice of C may influence the accuracy of the solution.

Acknowledgements

The authors are indebted to Mrs L. Parry for typing the paper and Mr R.A. Smith for help in figure preparation.

References

Blumberg, A. F., Mellor, G. L., 1987. A description of a three-dimensional coastal ocean circulation model. No. 4 in Coastal and Estuarine Sciences. American Geophysical Union, Washington, DC, p. 208pp.

Bolding, K., Burchard, H., Pohlmann, T., Stipps, A., 2002. Turbulent mixing in the northern North Sea: a numerical model study. Continental Shelf Research 22, 27072724.

Csanady, G. T., 1972. Response of large stratified lakes to wind. Journal of Physical Oceanography 2, 3–13.

Csanady, G. T., 1973. Transverse internal seiches in large oblong lakes and marginal seas. Journal of Physical Oceanography 3, 339–447.

Csanady, G. T., 1996. Circulation in the Coastal Ocean. D. Reidel Publishing Company, Boston.

Davies, A. M., 1980. Three dimensional hydrodynamic numerical models. Part 1. A homogeneous ocean-shelf model. Part 2. A stratified model of the Northern North Sea. Bergen University, Bergen, pp. 370–426.

Davies, A. M., Xing, J., 2003. Processes influencing wind induced current profiles in near coastal stratified regions. Continental Shelf Research 23, 1379–1400.

Davies, A. M., Xing, J., 2004. Modelling processes influencing windinduced internal wave generation and propagation. Continental Shelf Research 24, 22452271.

Goudsmit, G.-H., Burchard, H., Peeters, F., Wuest, A., 2002. Application of k-ϵ turbulence models to enclosed basins: The role of internal seiches. Journal of Geophysical Research 107, 3230, doi:10.1029/2001JC000954.

Heaps, N. S., 1980. Density currents in a two-layered coastal system, with application to the Norwegian Coastal Current. Geophysical Journal of the Royal Astronomical Society 63, 298310.

Heaps, N. S., Ramsbottom, A. E., 1966. Wind effects on the water in a narrow two-layered lake. Philosophical Transactions of the Royal Society of London 259, 391430.

James, I. D., 1996. Advection schemes for shelf sea models. Journal of Marine Systems 8, 237–254.

Luyten, P. J., Carniel, S., Umgiesser, G., 2002. Validation of turbulence closure parameterizations for stably stratified flows using the PROVESS turbulence measurements in the North Sea. Journal of Sea Research 47, 239–267.

Luyten, P. J., Deleersnijder, E., Ozer, J., Ruddick, K. G., 1996. Presentation of a family of turbulence closure models for stratified shallow water flows and preliminary application to the Rhine outflow region. Continental Shelf Research 16, 101–130.

Platzman, G. W., 1963. The dynamic prediction of wind tides on Lake Erie. Meteorological Monographs 4(26), 44.

Simons, T. J., 1978. Generation and propagation of downwelling fronts. Journal of Physical Oceanography 8, 571–581.

Smagorinsky, J., 1963. General circulation experiments with the primitive equations I. The basic experiment. Monthly Weather Review 91, 99–164.

Winant, C. D., 2004. Three-dimensional wind-driven flow in an elongated, rotating basin. Journal of Physical Oceanography 34, 462476.

Xing, J., Chen, F., Proctor, R., 1999. A two-dimensional slice model of the shelf edge region off the west coast of Scotland: model response to realistic seasonal forcing and the role of the M_2 tide. Continental Shelf Research 19, 13531386.

Xing, J., Davies, A. M., 1998. A three-dimensional model of internal tides on the Malin-Hebrides shelf and shelf edge. Journal of Geophysical Research 103(C) (12), 27821–27847.

Xing, J., Davies, A. M., 2001a. Non-linear effects of internal tides on the generation of the tidal mean flow at the Hebrides shelf edge. Geophysical Research Letters 28, 3939–3942.

Xing, J., Davies, A. M., 2001b. A three-dimensional baroclinic model of the Irish Sea: Formation of the thermal fronts and associated circulation. Journal of Physical Oceanography 31, 94–114.

Xing, J., Davies, A. M., 2005. Influence of a cold water bottom dome on internal wave trapping. Geophysical Research Letters 32, L03601, doi:10.1029/2004GLO21833.